

VISION-BASED ESTIMATION, LOCALIZATION, AND CONTROL OF AN
UNMANNED AERIAL VEHICLE

By

MICHAEL KENT KAISER

A DISSERTATION PRESENTED TO THE GRADUATE SCHOOL
OF THE UNIVERSITY OF FLORIDA IN PARTIAL FULFILLMENT
OF THE REQUIREMENTS FOR THE DEGREE OF
DOCTOR OF PHILOSOPHY

UNIVERSITY OF FLORIDA

2008

Copyright 2008

by

Michael Kent Kaiser

To my wife, Brigita, our daughters, MaryEllen Ann and Eliška Gaynor, and my
mother, Carole Campbell Kaiser.

ACKNOWLEDGMENTS

First and foremost, I would like to express my gratitude to Dr. Warren Dixon for not only providing me with exceptional guidance, encouragement, knowledge, and friendship, but also serving as an example of a quality person of high character - worthy of emulating!

I would also like to thank my committee members: Dr. Peter Ifju, Dr. Thomas Burks, Dr. Norman Fitz-Coy, and Dr. Naira Hovakimyan. It was a great honor to have them on my committee, each one carrying a specific meaning for me.

The NCR lab team is composed of a higher concentration of pure and lean talent than any single group of people I have ever worked with, which is why it was such a great privilege to be a member, albeit a little intimidating! I should point out that those individuals in the NCR group who made my degree possible are: Will MacKunis, Dr. Nick Gans, Dr. Guoqiang Hu, Parag Patre, and Sid Mehta.

And I would be remiss to not acknowledge the stabilizing "third leg" in my schooling endeavors; namely, the Air Force Research Laboratory Munitions Directorate (AFRL/RW) that provided the push and continued support for my education.

Also of note, the following individuals whom I have had the opportunity to work with as an engineer and who were either mentors or engineers to aspire to, or both are: Henry Yarborough, Walter J. "Jake" Klinar, Dr. Karolos Grigoriadis, Bob Loschke, Dr. Paul Bevilaqua, Dr. Leland Nicolai, John K. "Jack" Buckner, Dr. James Cloutier, and Dr. Anthony Calise.

Finally, I cannot forget to mention Ms. Judi Shivers at the REEF and all of the favors I owe her that I cannot possibly repay.

TABLE OF CONTENTS

	<u>page</u>
ACKNOWLEDGMENTS	iv
LIST OF FIGURES	vii
ABSTRACT	x
CHAPTER	
1 INTRODUCTION	1
1.1 Motivation	1
1.2 Dissertation Overview	6
1.3 Research Plan	6
2 AIRCRAFT MODELING AND SIMULATION	8
2.1 Introduction	8
2.2 Aerodynamic Characterization	9
2.3 Mass Property Estimation	9
2.4 Simulink Effort	13
2.5 Conclusions	17
3 AUTONOMOUS CONTROL DESIGN	18
3.1 Introduction	18
3.2 Baseline Controller	19
3.3 Robust Control Development	21
3.4 Control Development	24
3.4.1 Error System	25
3.4.2 Stability Analysis	28
3.5 Simulation Results	32
3.6 Conclusion	37
4 DAISY-CHAINING FOR STATE ESTIMATION	39
4.1 Introduction	39
4.2 Pose Reconstruction From Two Views	40
4.2.1 Euclidean Relationships	40
4.2.2 Projective Relationships	41
4.2.3 Chained Pose Reconstruction for Aerial Vehicles	42
4.2.4 Simulation Results	47

4.2.5	Experimental Results	49
4.3	Conclusions	61
5	LYAPUNOV-BASED STATE ESTIMATION	63
5.1	Introduction	63
5.2	Affine Euclidean Motion	63
5.3	Object Projection	66
5.4	Range Identification For Affine Systems	67
5.4.1	Objective	67
5.4.2	Estimator Design and Error System	68
5.5	Analysis	69
5.6	Conclusion	72
6	CONTRIBUTIONS AND FUTURE WORK	73
APPENDIX		
A	(CHAPTER 3) INTEGRATION OF THE AUXILIARY FUNCTION, $L(t)$	76
B	(CHAPTER 4) VIDEO EQUIPMENT USED ONBOARD THE AIR- CRAFT	77
C	(CHAPTER 4) GROUND SUPPORT EQUIPMENT	81
	REFERENCES	84
	BIOGRAPHICAL SKETCH	92

LIST OF FIGURES

<u>Figure</u>	<u>page</u>
2-1 LinAir wireframe representation of the Osprey airframe.	9
2-2 Simulink modeling of aerodynamic coefficients.	10
2-3 Measurable inertia values of the Osprey airframe.	12
2-4 Simulink representation of the aircraft equations of motion.	15
2-5 Simulink aircraft equations of motion sub-block: Rotational EOM.	15
2-6 Simulink aircraft equations of motion sub-block: Body Rates to Euler Angle Rates.	16
2-7 Simulink aircraft equations of motion sub-block: Translational EOM.	16
3-1 Photograph of the Osprey aircraft testbed.	18
3-2 Rudimentary control system used for proof of concept for vision-based extimation algorithms.	20
3-3 Plot of the discrete vertical (upward) wind gust used in the controller simulation.	34
3-4 Illustration of uncoupled velocity and pitch rate response during closed- loop longitudinal controller operation.	36
3-5 Illustration of uncoupled roll rate and yaw rate response during closed- loop lateral controller operation.	37
4-1 Euclidean relationships between two camera poses.	41
4-2 Illustration of pose estimation chaining.	44
4-3 Depth estimation from altitude.	45
4-4 Actual translation versus estimated translation where the estimation is not part of the closed-loop control.	48
4-5 Actual attitude versus estimated attitude where the estimation is not part of the closed-loop control.	48
4-6 Autononmous control architecture.	50

4-7	Actual translation versus estimated translation where the estimated value is used within the closed-loop control.	50
4-8	Actual attitude versus estimated attitude where the estimated value is used within the closed-loop control.	51
4-9	Overview of the flight test system and component interconnections.	52
4-10	Single video frame with GPS overlay illustrating landmarks placed along inside edge of the runway.	52
4-11	Experimental flight test results. Estimated position compared to two GPS signals.	53
4-12	Technique for achieving accurate landmark relative placement distances.	54
4-13	Single video frame from second flight test experiment illustrating the effect of the more forward looking, wider field of view camera.	55
4-14	Single video frame from second flight test experiment with the lens distortion removed.	56
4-15	Example of a 3D color contour plot generated from the matrix designed as a nonlinear combination of the red and green color space matrices.	57
4-16	Image plane trajectories made by the landmarks from patch 1 entering and exiting the field of view.	58
4-17	Basic concept of geometric position reconstruction from known landmark locations.	60
4-18	Illustration of how four tetrahedrons are used to estimate the length of each edge, a , b , c , & d three times.	61
4-19	Second experimental flight test results. Estimated position compared to more accurate position from geometric reconstruction technique.	62
5-1	Moving camera stationary object scenario.	65
5-2	Euclidean point projected onto image plane of a pinhole camera	65
B-1	Sony Color Exview SuperHAD (480 Lines of Resolution)	77
B-2	Panasonic AG-DV1 Digital Video Recorder	78
B-3	Garmin GPS 35 OEM GPS Receiver	78
B-4	Intuitive Circuits, LLC - OSD-GPS Overlay Board	79
B-5	12V, 2.4Ghz, 100mW, Video Transmitter and Antennae	79

B-6	Eagle Tree, Seagull, Wireless Dashboard Flight System - Pro Version: (1) Wireless Telemetry Transmitter, (2) Eagle Tree Systems G-Force Expander, and (3) Eagle Tree Systems GPS Expander	80
C-1	RX-2410 2.4 GHz Wireless 4-channel Audio/Video Selectable Receiver	81
C-2	Sony GV-D1000 Portable MiniDV Video Walkman	82
C-3	Eagle Tree, Seagull, Real-time Data Dashboard, Wireless Telemetry Data, Receiver Model STR-01	82
C-4	Leica DISTO™ A5 (Measuring Range up to 650 ft, Accuracy +/- 0.06 inches)	83

Abstract of Dissertation Presented to the Graduate School
of the University of Florida in Partial Fulfillment of the
Requirements for the Degree of Doctor of Philosophy

VISION-BASED ESTIMATION, LOCALIZATION, AND CONTROL OF AN
UNMANNED AERIAL VEHICLE

By

Michael Kent Kaiser

May 2008

Chair: Dr. Warren E. Dixon
Major: Aerospace Engineering

Given the advancements in computer vision and estimation and control theory, monocular camera systems have received growing interest as a local alternative/collaborative sensor to GPS systems. One issue that has inhibited the use of a vision system as a navigational aid is the difficulty in reconstructing inertial measurements from the projected image. Current approaches to estimating the aircraft state through a camera system utilize the motion of feature points in an image. One geometric approach that is in this dissertation uses a series of homography relationships to estimate position and orientation with respect to an inertial pose. This approach creates a series of “daisy-chained” pose estimates in which the current feature points can be related to previously viewed feature points to determine the current coordinates between each successive image. Because this technique relies on the accuracy of a depth estimation, a Lyapunov-based range identification method is developed that is intended to enhance and compliment the homography based method.

The nature of the noise associated with using a camera as a position and orientation sensor is distinctly different from that of legacy type sensors used for air

vehicles such as accelerometers, rate gyros, attitude resolvers, etc. In order to fly an aircraft in a closed-loop sense, using a camera as a primary sensor, the controller will need to be robust to not only parametric uncertainties, but to system noise that is of the kind uniquely characteristic of camera systems. A novel nonlinear controller, capable of achieving asymptotic stability while rejecting a broad class of uncertainties, is developed as a plausible answer to such anticipated issues.

A commercially available vehicle platform is selected to act as a testbed for evaluating a host of image-based methodologies as well as evaluating advanced control concepts. To enhance the vision-based analysis as well as control system design analysis, a simulation of this particular aircraft is also constructed. The simulation is intended to be used as a tool to provide insight into algorithm feasibility as well as to support algorithm development, prior to physical integration and flight testing.

The dissertation will focus on three problems of interest: 1) vehicle state estimation and control using a homography-based daisy-chaining approach; 2) Lyapunov-based nonlinear state estimation and range identification using a pinhole camera; 3) robust aerial vehicle control in the presence of structured and unstructured uncertainties.

CHAPTER 1 INTRODUCTION

1.1 Motivation

Feedback linearization is a general control method where the nonlinear dynamics of a system are canceled by state feedback yielding a residual linear system. Dynamic inversion is a similar concept as feedback linearization that is commonly used within the aerospace community to replace linear aircraft dynamics with a reference model [1–11]. For example, a general dynamic inversion approach is presented in [4] for a reference tracking problem for a minimum-phase and left-invertible linear system. A dynamic inversion controller is designed for a nonminimum-phase hypersonic aircraft system in [2], which utilizes an additional controller to stabilize the zero dynamics. A finite-time stabilization design is proposed in [3], which utilizes dynamic inversion given a full rank input matrix. Typically, dynamic inversion methods (e.g., [1, 2]) assume the corresponding plant models are exactly known. However, parametric uncertainty, additive disturbances, and unmodeled plant dynamics are always present in practical systems.

Motivated by the desire to improve the robustness to uncertainty over traditional methods, adaptive dynamic inversion (ADI) was developed as a method to compensate for parametric uncertainty (cf. [4, 6, 7, 10]). Typically, ADI methods exploit model reference adaptive control (MRAC) techniques where the desired input-output behavior of the closed-loop system is given via the corresponding dynamics of a reference model [5, 7, 12]. Therefore, the basic task is to design a controller which will ensure the minimal error between the reference model and the plant outputs despite uncertainties in the plant parameters and working conditions.

Several efforts (e.g., [8–10, 13–16]) have been developed for the more general problem where the uncertain parameters or the inversion mismatch terms do not satisfy the linear-in-the-parameters assumption (i.e., non-LP). One method to compensate for non-LP uncertainty is to exploit a neural network as an on-line function approximation method as in [13–15]; however, all of these results yield uniformly ultimately bounded stability due to the inherent function reconstruction error.

In contrast to neural network-based methods to compensate for the non-LP uncertainty, a robust control approach was recently developed in [17] (coined RISE control in [18]) to yield an asymptotic stability result. The RISE-based control structure has been used for a variety of fully actuated systems in [17–25]. The contribution in this result is the use of the RISE control structure to achieve asymptotic output tracking control of a model reference system, where the plant dynamics contain a bounded additive disturbance (e.g., potential disturbances include: gravity, inertial coupling, nonlinear gust modeling, etc.). This result represents the first ever application of the RISE method where the controller is multiplied by a non-square matrix containing parametric uncertainty. To achieve the result, the typical RISE control structure and closed-loop error system development is modified by adding a robust control term, which is designed to compensate for the uncertainty in the input matrix. The result is proven via Lyapunov-based stability analysis and demonstrated through numerical simulation.

GPS (Global Positioning System) is the primary navigational sensor modality used for vehicle guidance, navigation, and control. However, a comprehensive study referred to as the Volpe Report [26] indicates several vulnerabilities of GPS associated with signal disruptions. The Volpe Report delineates the sources of interference with the GPS signal into two categories, unintentional and deliberate disruptions. Some of the unintentional disruptions include ionosphere interference (also known as ionospheric scintillation) and radio frequency interference

(broadcast television, VHF, cell phones, two-way pagers); whereas, some of the intentional disruptions involve jamming, spoofing, and meaconing. Some of the ultimate recommendations of this report were to, “create awareness among members of the domestic and global transportation community of the need for GPS backup systems...” and to “conduct a comprehensive analysis of GPS backup navigation...” which included ILS (Instrument Landing Systems), LORAN (Long Range Navigation), and INS (Inertial Navigation Systems) [26].

The Volpe report acted as an impetus to investigate mitigation strategies for the vulnerabilities associated with the current GPS navigation protocol, nearly all following the suggested GPS backup methods that revert to archaic/legacy methods. Unfortunately, these navigational modalities are limited by the range of their land-based transmitters, which are expensive and may not be feasible for remote or hazardous environments. Based on these restrictions, researchers have investigated local methods of estimating position when GPS is denied.

Given the advancements in computer vision and estimation and control theory, monocular camera systems have received growing interest as a local alternative/collaborative sensor to GPS systems. One issue that has inhibited the use of a vision system as a navigational aid is the difficulty in reconstructing inertial measurements from the projected image. Current approaches to estimating the aircraft state through a camera system utilize the motion of feature points in an image. A geometric approach is proposed in this dissertation that uses a series of homography relationships to estimate position and orientation with respect to an inertial pose. This approach creates a series of “daisy-chained” pose estimates [27, 28] in which the current feature points can be related to previously viewed feature points to determine the current coordinates between each successive image. Through these relationships, previously recorded GPS data can be linked with the image data to provide measurements of position and attitude (i.e. pose)

in navigational regions where GPS is denied. The method also delivers an accurate estimation of vehicle attitude, which is an open problem in aerial vehicle control. The estimation method can be executed in real time, making it amenable for use in closed loop guidance control of an aircraft.

The concept of vision-based control for a flight vehicle has been an active area of research over the last decade. Recent research literature on the subject of vision-based state estimation for use in control of a flight vehicle can be categorized by several distinctions. One distinction is that some methods rely heavily on simultaneous sensor fusion [29] while other methods rely solely on camera feedback [30]. Research can further be categorized into methods that require a priori knowledge of landmarks (such as pattern or shape [31–36], light intensity variations [37], runway edges or lights [38–40]) versus techniques that do not require any prior knowledge of landmarks [41–47]. Another category of research includes methods that require the image features to remain in the field-of-view [41] versus methods that are capable of acquiring new features [42]. Finally, methods can be categorized according to the vision-based technique for information extraction such as: Optic Flow [48], Simultaneous Localization And Mapping (SLAM) [43], Stereo Vision [49], Epipolar Geometry [34, 41, 45, 46]. This last category might also be delineated between methods that are more computationally intensive and therefore indicative of the level of real-time on-board computational feasibility.

Methods using homography relationships between images to estimate the pose of an aircraft are presented by Caballero et al. [46] and Shakernia et al. [41] (where it is referred to as the “planar essential matrix”). The method presented by Caballero et al. is limited to flying above a planar environment and creates an image mosaic, which can be costly in terms of memory. Shakernia’s approach, does not account for feature points entering and exiting the camera field of view. The method introduced in this dissertation proposes a solution which allows points to

continuously move into and out of the camera field of view. The requirement of flying over a constant planar surface is also relaxed to allow flight over piecewise planar patches, more characteristic of real world scenarios.

Reconstructing the Euclidean coordinates of observed feature points is a challenging problem of significant interest, because range information (i.e., the distance from the imaging system to the feature point) is lost in the image projection. Different tools (e.g., extended Kalman filter, nonlinear observers) have been used to address the structure and/or motion recovery problem from different points of view. Some researchers (e.g., see [50–53]) have applied the extended Kalman filter (EKF) to address the structure/motion recovery problem. In order to use the EKF method, a priori knowledge of the noise distribution is required, and the motion recovery algorithm is developed based on the linearization of the nonlinear vision-based motion estimation problem.

Due to restrictions with linear methods, researchers have developed various nonlinear observers (e.g., see [54–58]). For example, several researchers have investigated the range identification problem for conventional imaging systems when the motion parameters are known. In [57], Jankovic and Ghosh developed a discontinuous observer, known as the Identifier Based Observer (IBO), to exponentially identify range information of features from successive images of a camera where the object model is based on known skew-symmetric affine motion parameters. In [55], Chen and Kano generalized the object motion beyond the skew-symmetric form of [57] and developed a new discontinuous observer that exponentially forced the state observation error to be uniformly ultimately bounded (UUB). In comparison to the UUB result of [55], a continuous observer was constructed in [56] to asymptotically identify the range information for a general affine system with known motion parameters. That is, the result in [56] eliminated the skew-symmetric assumption and yielded an asymptotic result with a continuous

observer. More recently, a state estimation strategy was developed in [59, 60] for affine systems with known motion parameters where only a single homogeneous observation point is provided (i.e., a single image coordinate). In [58], a reduced order observer was developed to yield a semi-global asymptotic stability result for a fixed camera viewing a moving object with known motion parameters for a pinhole camera.

1.2 Dissertation Overview

In this dissertation, vision-based estimation, localization, and control methodologies are proposed for an autonomous air vehicle flying over what are nominally considered as planar patches of feature points. The dissertation will focus on four problems of interest: 1) develop a robust control system resulting in a semi-global asymptotic stable system for an air vehicle with structured and unstructured uncertainties; 2) provide a means of state estimation where feature points can continuously enter and exit the field-of-view, as would nominally be the case for a fixed-wing vehicle, via a novel daisy-chaining approach;. 3) introduce a vision-based altimeter which seeks to resolve the depth ambiguity, which is a current issue with the homography based daisy-chaining method that uses an altimeter to provide a depth measurement.

1.3 Research Plan

This chapter serves as an introduction. The motivation, problem statement and the proposed research plan of the dissertation is provided in this chapter.

Chapter 2 describes a from-the-ground-up simulation development of a research air vehicle specifically selected for its performance capabilities for flight testing of vision-based, estimation, localization, and control methodologies. An outcome from this chapter is a fully nonlinear simulation of a commercially available mini-aircraft that can be used for a wide range of analysis and design purposes.

Chapter 3 presents an inner-loop robust control method, providing mathematical theory and simulation results. The contribution of the development in this chapter is a controller that is asymptotically stable for a broad class of model uncertainties as well as bounded additive disturbances.

Chapter 4 involves the development of the daisy-chaining method as a viable GPS backup technology as well as a state estimation procedure. Results are demonstrated via simulation as well as flight testing. The contribution from this chapter is in developing a means for an aircraft to perform position and orientation estimation from planar feature point patches that enter and leave the field of view, indefinitely.

Chapter 5 investigates a nonlinear estimator that can provide an alternate means to altitude estimation as well as to provide alternate state estimation. The results of this chapter is that it develops a Lyapunov-based nonlinear state estimator using a pinhole camera that could work in symbiosis with the homography-based daisy chaining technique and it also suggests how, at least notionally, the camera can therefore be used as a sole sensor onboard an aircraft.

CHAPTER 2 AIRCRAFT MODELING AND SIMULATION

2.1 Introduction

A vehicle simulation has been developed to investigate the feasibility of the proposed vision-based state estimation and guidance method. The Osprey fixed wing aerial vehicle, by Air and Sea Composites, Inc. (see Figure 4-3) was selected for evaluating a host of image-based methodologies as well as for potentially evaluating advanced control concepts. This particular aircraft was chosen for several reasons; chiefly being: low cost, pusher prop being amenable to forward looking camera placement, and payload capability. A fully nonlinear model of the equations of motion and aerodynamics of the Osprey are constructed within the Simulink framework. A nonlinear model, as opposed to linear model, is preferred in this analysis as it better represents the coupled dynamics and camera kinematics, which could potentially stress the performance and hence, feasibility of the pose estimation algorithm.

The first undertaking of the dissertation is to develop a fully nonlinear, six degrees-of-freedom model of the Osprey aircraft. The simulation will provide a means to test proof-of-concept methodologies prior to testing on the actual Osprey testbed. For example, a specific maneuver can be created within the simulation environment to perform a simultaneous rolling, pitching, and yawing motion of the aircraft combined with a fixed mounted camera to test the robustness of the vision-based algorithm.

A commercially available vehicle platform is selected to act as a testbed for evaluating a host of image-based methodologies as well as evaluating advanced control concepts.

```

Element Geometry
Element # 1
XRootLE -4.62000
YRootLE -66.12500
ZRootLE 0.00000
XRootTE 7.69000
YRootTE -66.12500
ZRootTE -0.64300
XTipLE -4.62000
YTipLE 66.12500
ZTipLE 0.00000
XTipTE 7.69000
YTipTE 66.12500
ZTipTE -0.64300
# Panels: 20
CD0: 0.01000
CD1: 0.00000
CD2: 0.00000
Cmac: 0.00000
CLmax: 1.60000

```

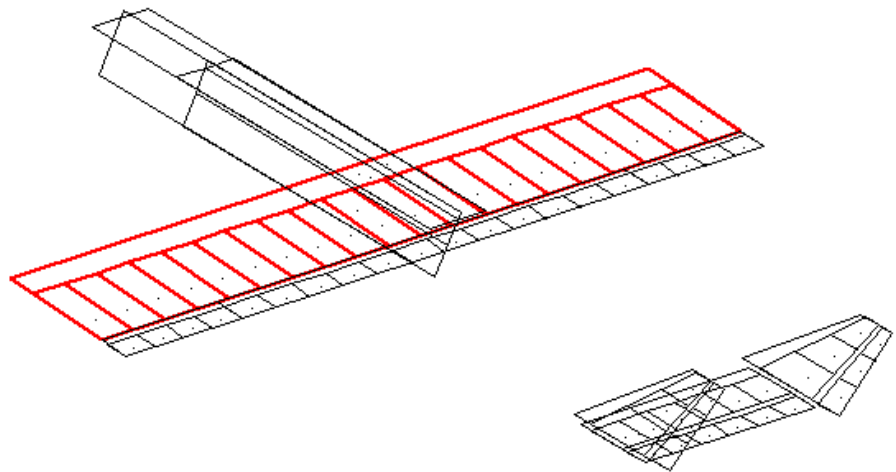


Figure 2-1: LinAir wireframe representation of the Osprey airframe.

2.2 Aerodynamic Characterization

The development of the vehicle simulation entailed two primary tasks, estimating the aerodynamic characteristics and evaluating the mass properties. The aerodynamic characterization of the Osprey aircraft was computed using LinAir, by Desktop Aeronautics, Inc., which employs the discrete vortex Weissinger method (i.e. extended lifting line theory), to solve the subsonic, inviscid, irrotational Prandtl-Glauert equation [61]. Lifting surfaces are modeled by discrete horseshoe vortices where each makes up one panel, panels make up an element, and elements are grouped to make up the aircraft geometry as shown in Figure 2-1. The resulting nondimensional, aerodynamic coefficients are implemented via Simulink's multi-dimensional lookup tables as illustrated in Figure 2-2.

2.3 Mass Property Estimation

The inertia and mass properties of the aircraft were measured using a precision mass, center of gravity, and moment of inertia (MOI) instrument. The instrument is comprised of a table levitated on a gas bearing pivot and a torsional rod connected to the center of the table, resulting in a torsion pendulum for MOI measurement. Because the vehicle could not be mounted on its nose or tail, an

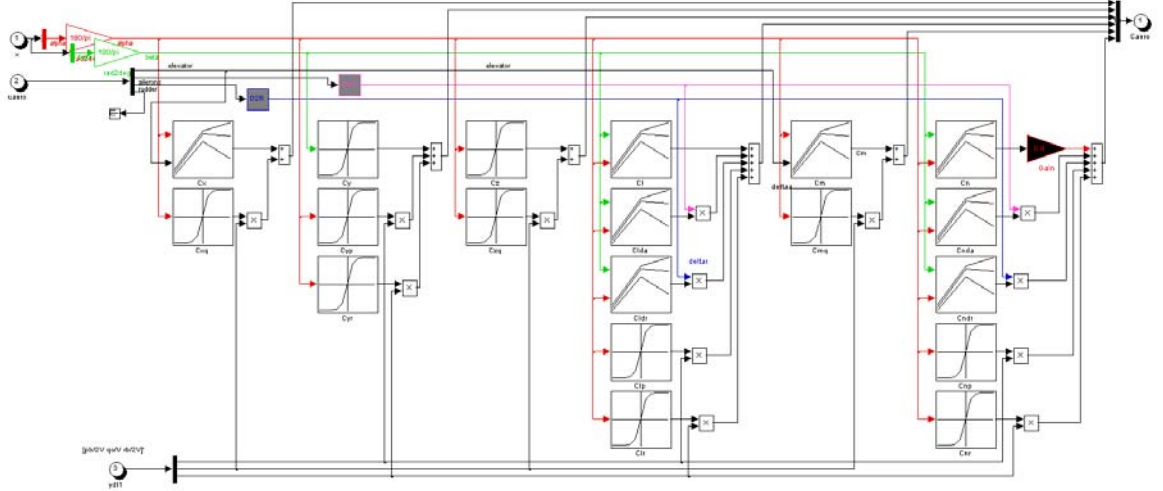


Figure 2-2: Simulink modeling of aerodynamic coefficients.

alternate method was devised to estimate the vehicle's roll inertia, I_{xx} . Given that the angular momentum in one frame, A is related to angular momentum in a second frame, B via a simple coordinate transformation, T_B^A (read as transformation from frame B to frame A), the following series of relationships can be written

$$\begin{aligned}
 H^A &= T_B^A H^B = T_B^A [I^B \omega^B] \\
 &= T_B^A [I^B (T_A^B T_B^A) \omega^B] && \text{where } (T_A^B T_B^A) = I \\
 &= T_B^A [I^B T_A^B (T_B^A \omega^B)] && \text{where } (T_B^A \omega^B) = \omega^A \\
 &= T_B^A I^B T_A^B \omega^A.
 \end{aligned}$$

The inertia relationship between two frames is given by, $I^B = T_B^A I^A T_A^B$, which for this particular case of estimating the roll inertia is expressed as

$$\begin{bmatrix} I_{xx} & 0 & I_{xz} \\ 0 & I_{yy} & 0 \\ I_{xz} & 0 & I_{zz} \end{bmatrix} = \begin{bmatrix} c\theta & 0 & -s\theta \\ 0 & 1 & 0 \\ s\theta & 0 & c\theta \end{bmatrix} \begin{bmatrix} I'_{xx} & 0 & I'_{xz} \\ 0 & I'_{yy} & 0 \\ I'_{xz} & 0 & I'_{zz} \end{bmatrix} \begin{bmatrix} c\theta & 0 & s\theta \\ 0 & 1 & 0 \\ -s\theta & 0 & c\theta \end{bmatrix} \quad (2-1)$$

Expanding this equation

$$\begin{bmatrix} I_{xx} & 0 & I_{xz} \\ 0 & I_{yy} & 0 \\ I_{xz} & 0 & I_{zz} \end{bmatrix} = \begin{bmatrix} I'_{xx} \cos^2(\theta) - I'_{xz} \sin(2\theta) \dots & 0 & I'_{xx} \frac{\sin(2\theta)}{2} + I'_{xz} \cos(2\theta) \dots \\ & + I'_{zz} \sin^2(\theta) & -I'_{zz} \frac{\sin(2\theta)}{2} \\ 0 & I'_{yy} & 0 \\ I'_{xx} \frac{\sin(2\theta)}{2} + I'_{xz} \cos(2\theta) \dots & 0 & I'_{xx} \sin^2(\theta) + I'_{xz} \sin(2\theta) \dots \\ & -I'_{zz} \frac{\sin(2\theta)}{2} & +I'_{zz} \cos^2(\theta) \end{bmatrix} \quad (2-2)$$

From this, it is noted that $I_{yy} = I'_{yy}$, as expected. Furthermore, because the airframe is mostly symmetrical about its x - y plane, see Figure 2-3, it is reasonable to assume that $I_{xz} \approx 0$. Notice also that since the matrix in (2-2) is symmetric, it is only necessary to look at the upper or lower triangular elements. Separating the known terms on the right-hand-side and unknown terms on the left-hand-side gives the following equalities

$$\begin{aligned} I_{xx} - I'_{xx} \cos^2(\theta) + I'_{xz} \sin(2\theta) &= I'_{zz} \sin^2(\theta) \\ -I'_{xx} \sin^2(\theta) - I'_{xz} \sin(2\theta) &= -I_{zz} + I'_{zz} \cos^2(\theta) \\ I'_{xx} \frac{\sin(2\theta)}{2} + I'_{xz} \cos(2\theta) &= I'_{zz} \frac{\sin(2\theta)}{2} \end{aligned} \quad (2-3)$$

Rewriting in matrix form, the unknown terms are solved for accordingly

$$\begin{Bmatrix} I_{xx} \\ I'_{xx} \\ I'_{xz} \end{Bmatrix} = \begin{bmatrix} 1 & -\cos^2(\theta) & \sin(2\theta) \\ 0 & -\sin^2(\theta) & -\sin(2\theta) \\ 0 & \frac{\sin(2\theta)}{2} & \cos(2\theta) \end{bmatrix}^{-1} \begin{Bmatrix} I'_{zz} \sin^2(\theta) \\ -I_{zz} + I'_{zz} \cos^2(\theta) \\ I'_{zz} \frac{\sin(2\theta)}{2} \end{Bmatrix} \quad (2-4)$$

The known terms in (2-4) are I'_{zz} , I_{zz} , and θ , where θ is as depicted in Figure 2-3. Therefore, the complete inertia properties can be calculated from the only 3 measurements possible, as illustrated in Figure 2-3.

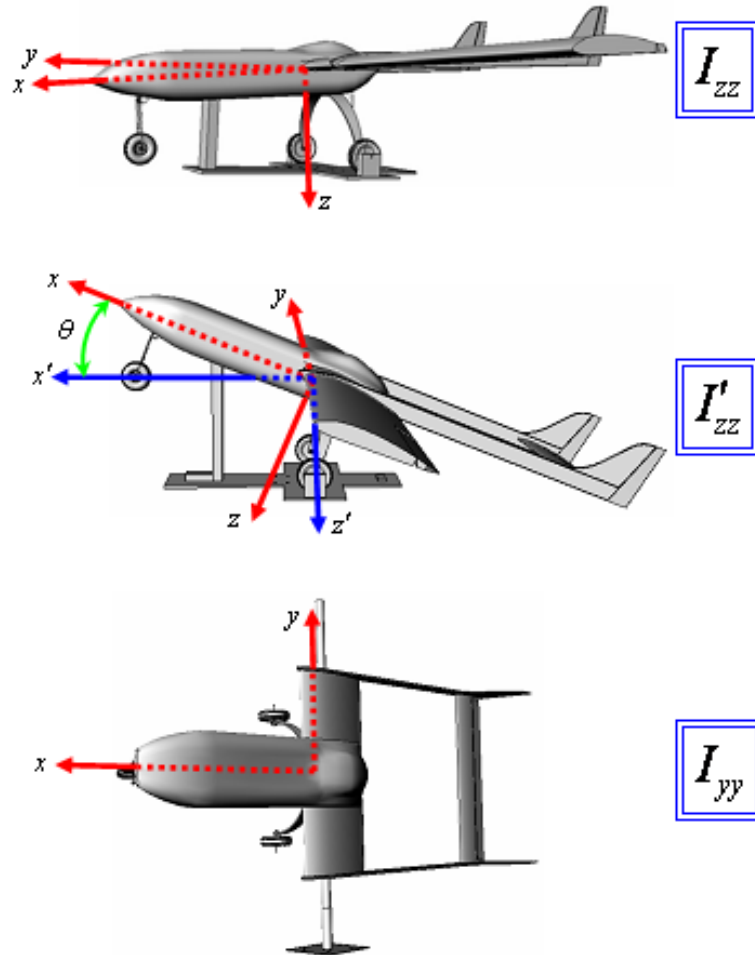


Figure 2-3: Measurable inertia values of the Osprey airframe.

2.4 Simulink Effort

The core of the simulation uses the aforementioned aerodynamics and mass properties along with the following nonlinear translational and rotational rigid body equations of motion derived in the vehicle body-axis system

$$\dot{u} = \frac{1}{m}F_x(V, \rho, \alpha, q, \delta_{elev}, \delta_{throt}) - qw + rv - g \sin(\theta) \quad (2-5)$$

$$\dot{v} = \frac{1}{m}F_y(V, \rho, \alpha, \beta, p, r) - ru + pw + g \cos(\theta) \sin(\phi) \quad (2-6)$$

$$\dot{w} = \frac{1}{m}F_z(V, \rho, \alpha, q) - pv + qu + g \cos(\theta) \cos(\phi) \quad (2-7)$$

and

$$\begin{aligned} \dot{p} = & \frac{I_{zz}}{I_{xx}I_{zz} - I_{xz}^2}M_x(V, \rho, \alpha, \beta, p, r, \delta_{rud}, \delta_{ail}) + \frac{I_{zz}}{I_{xx}I_{zz} - I_{xz}^2} \{-qr(I_{zz} - I_{yy}) + I_{xz}pq\} \dots \\ & + \frac{I_{xz}}{I_{xx}I_{zz} - I_{xz}^2}M_z(V, \rho, \alpha, \beta, p, r, \delta_{rud}, \delta_{ail}) + \frac{I_{xz}}{I_{xx}I_{zz} - I_{xz}^2} \{-pq(I_{yy} - I_{xx}) - I_{xz}qr\} \end{aligned} \quad (2-8)$$

$$\dot{q} = \frac{1}{I_y}M_y(V, \rho, \alpha, q, \delta_{elev}) - rp(I_{xx} - I_{zz}) - I_{xz}(p^2 - r^2) \quad (2-9)$$

$$\begin{aligned} \dot{r} = & \frac{I_{xz}}{I_{xx}I_{zz} - I_{xz}^2}M_x(V, \rho, \alpha, \beta, p, r, \delta_{rud}, \delta_{ail}) + \frac{I_{xz}}{I_{xx}I_{zz} - I_{xz}^2} \{-qr(I_{zz} - I_{yy}) + I_{xz}pq\} \dots \\ & + \frac{I_{xx}}{I_{xx}I_{zz} - I_{xz}^2}M_z(V, \rho, \alpha, \beta, p, r, \delta_{rud}, \delta_{ail}) + \frac{I_{xx}}{I_{xx}I_{zz} - I_{xz}^2} \{-pq(I_{yy} - I_{xx}) - I_{xz}qr\} \end{aligned} \quad (2-10)$$

where M and F represent the aerodynamic and propulsive moments and forces in body axis, given in x , y , & z components; I and m represent the vehicle's inertia tensor values and mass; V and ρ are relative velocity and air density; α and β are angle of attack and sideslip angle; p , q , and r are angular body rates; u , v , and w are translational velocities in the body frame; and δ represents the individual

control deflections. The corresponding kinematic relationships are given by

$$\begin{bmatrix} \dot{X} \\ \dot{Y} \\ \dot{Z} \end{bmatrix} = \begin{bmatrix} c\theta c\psi & s\phi s\theta c\psi - c\phi s\psi & c\phi s\theta c\psi + s\phi s\psi \\ c\theta s\psi & s\phi s\theta s\psi + c\phi c\psi & c\phi s\theta s\psi - s\phi c\psi \\ -s\theta & s\phi c\theta & c\phi c\theta \end{bmatrix} \begin{bmatrix} u \\ v \\ w \end{bmatrix} \quad (2-11)$$

and

$$\begin{bmatrix} \dot{\phi} \\ \dot{\theta} \\ \dot{\psi} \end{bmatrix} = \begin{bmatrix} 1 & \sin \phi \tan \theta & \cos \phi \tan \theta \\ 0 & \cos \phi & -\sin \phi \\ 0 & \sin \phi \sec \theta & \cos \phi \sec \theta \end{bmatrix} \begin{bmatrix} p \\ q \\ r \end{bmatrix} \quad (2-12)$$

where $c\psi$ and $s\psi$ denote $\cos(\psi)$ and $\sin(\psi)$, respectively (similarly for ϕ and θ).

The equations of motion and all simulation subsystems are constructed using standard Simulink library blocks, where no script files are incorporated, as shown in Figure 2-4.

The sub-blocks of interest depicted in the equations of motion model given in Figure 2-4 are: “Rotational EOM”, “Body Rates to Euler Angle Rates”, and “Translational EOM”, and are illustrated in Figures 2-5, 2-6, and 2-7, respectively.

Besides using the model given in Figure 2-4 for cases where a fully nonlinear simulation is required, it can also be used to generate linearized representations of the Osprey by utilizing Matlab’s linearizing capability. For example, the trimmed vehicle at a 60 meter altitude at 25 meters/sec. would have the corresponding state space representation

$$\begin{bmatrix} \dot{V} \\ \dot{\alpha} \\ \dot{q} \\ \dot{\theta} \end{bmatrix} = \begin{bmatrix} -0.15 & 11.08 & 0.08 & -9.81 \\ -0.03 & -7.17 & 0.83 & 0 \\ 0 & -37.35 & -9.96 & 0 \\ 0 & 0 & 1.00 & 0 \end{bmatrix} \begin{bmatrix} V \\ \alpha \\ q \\ \theta \end{bmatrix} + \begin{bmatrix} 3E^{-3} & 0.06 \\ 1E^{-5} & 1E^{-4} \\ -0.98 & 0 \\ 0 & 0 \end{bmatrix} \begin{bmatrix} \delta_{elevator} \\ \delta_{thrust} \end{bmatrix} \quad (2-13)$$

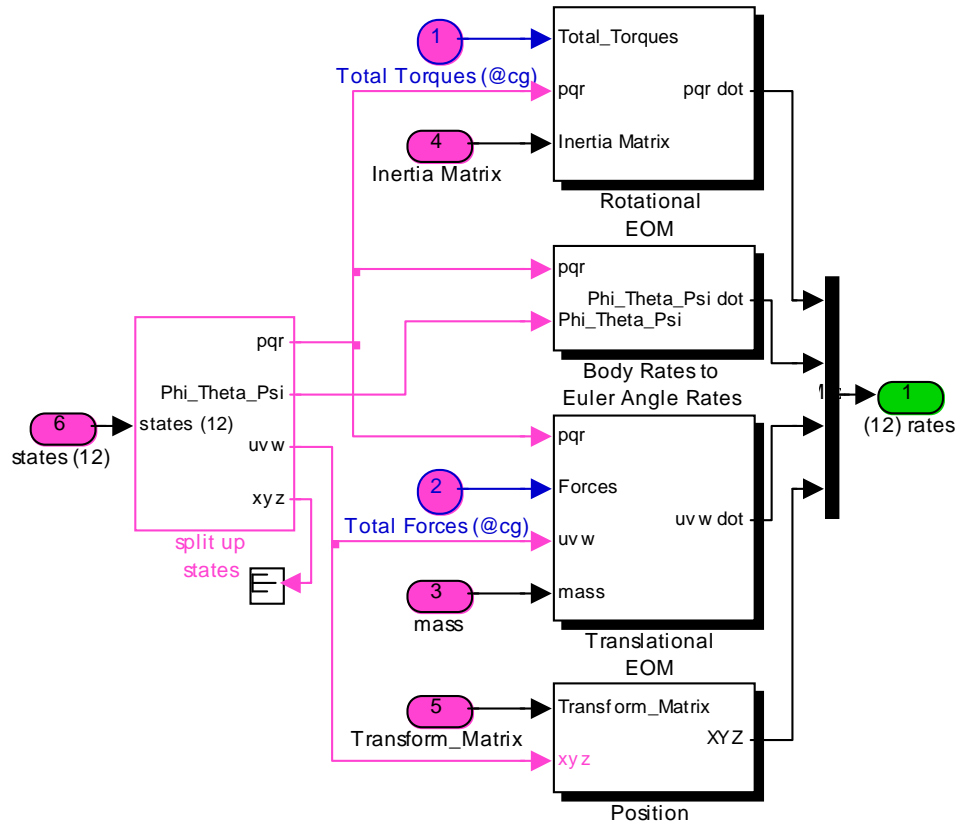


Figure 2-4: Simulink representation of the aircraft equations of motion.

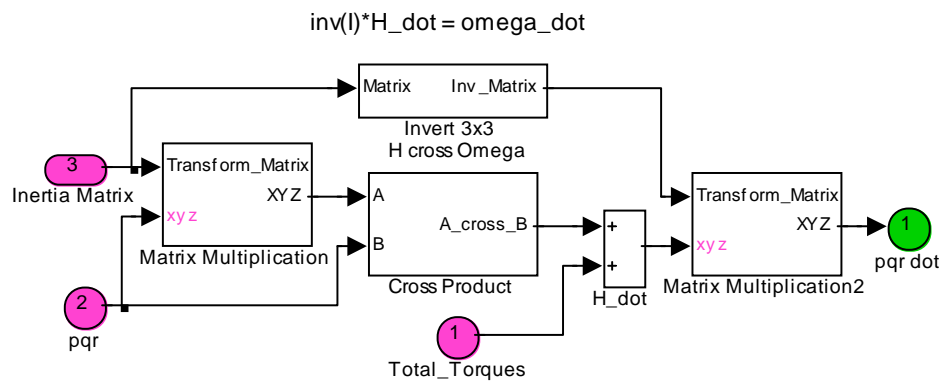


Figure 2-5: Simulink aircraft equations of motion sub-block: Rotational EOM.

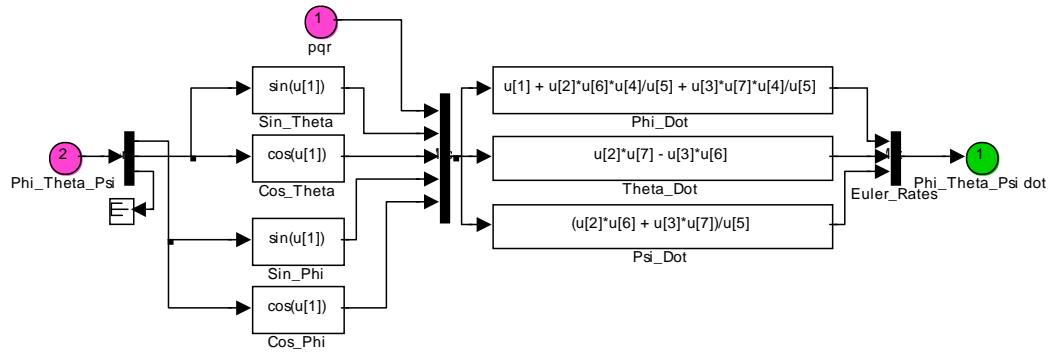


Figure 2–6: Simulink aircraft equations of motion sub-block: Body Rates to Euler Angle Rates.

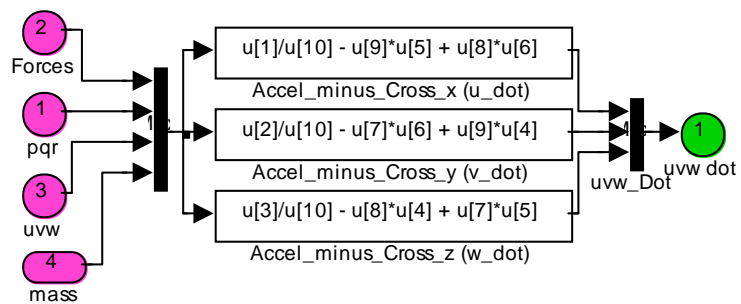


Figure 2–7: Simulink aircraft equations of motion sub-block: Translational EOM.

And the corresponding lateral state-space representation is computed to be

$$\begin{bmatrix} \dot{\beta} \\ \dot{p} \\ \dot{r} \\ \dot{\phi} \end{bmatrix} = \begin{bmatrix} -0.69 & -0.03 & -0.99 & 0.39 \\ -3.13 & -12.92 & 1.10 & 0 \\ 17.03 & -0.10 & -0.97 & 0 \\ 0 & 1.00 & -0.03 & 0 \end{bmatrix} \begin{bmatrix} \beta \\ p \\ r \\ \phi \end{bmatrix} + \begin{bmatrix} 0 & 0 \\ 1.50 & -0.02 \\ -0.09 & 0.17 \\ 0 & 0 \end{bmatrix} \begin{bmatrix} \delta_{aileron} \\ \delta_{rudder} \end{bmatrix} \quad (2-14)$$

where

$$\begin{bmatrix} V = \text{m/sec} \\ \alpha = \text{rad} \\ q = \text{rad/sec} \\ \theta = \text{rad} \end{bmatrix}, \quad \begin{bmatrix} \beta = \text{rad} \\ p = \text{rad/sec} \\ r = \text{rad/sec} \\ \phi = \text{rad} \end{bmatrix}, \quad \text{and} \quad \begin{bmatrix} \delta_{elevator} = \text{deg} \\ \delta_{thrust} = \text{N} \\ \delta_{aileron} = \text{deg} \\ \delta_{rudder} = \text{deg} \end{bmatrix}$$

This model would provide useful information in regards to intermediate feasibility of the vision-based method, such as providing insight into motion and frequency issues which can severely affect the performance of the vision-based methods. It can also serve as a basis for rudimentary control design, in the case where the flight regime is benign and hence, does not require emphasize the effect of vision-based state estimation in regards to vehicle control.

2.5 Conclusions

The efforts in this chapter illustrated the ground up development of a fully nonlinear simulation representing an aircraft testbed to host flight testing of image-based estimation and control algorithms. A method was devised to estimate the vehicle's roll inertia properties based upon the fact that the vehicle, unlike most airframes, is relatively symmetrical about its x - y plane. Finally, while the aerodynamic parameter estimates are derived from commercially available vortex lattice software, this type of code is very beneficial in time and cost savings, but it comes at the cost of model uncertainty; which yet again calls for control algorithms that are inherently robust.

CHAPTER 3 AUTONOMOUS CONTROL DESIGN

3.1 Introduction

A robust control approach was recently developed in [17] that exploits a unique property of the integral of the sign of the error (coined RISE control in [18]) to yield an asymptotic stability result. The RISE based control structure has been used for a variety of fully actuated systems in [17], [18], [62]. The contribution of this result is the ability to achieve asymptotic tracking control of a model reference system for not only a broad class of model uncertainties, but also for where the plant dynamics contain a bounded additive disturbance (e.g., potential disturbances include: dynamic inversion mismatch, wind gusts, nonlinear dynamics, etc.). In addition, this result represents the first ever application of the RISE method where the controller is multiplied by a non-square matrix containing parametric uncertainty and nonlinear, non-LP disturbances. The feasibility of this technique is proven through a Lyapunov-based stability analysis and through numerical simulation results.



Figure 3–1: Photograph of the Osprey aircraft testbed.

3.2 Baseline Controller

As mentioned, the vision-based estimation method that will be discussed further in chapter 4 was experimentally demonstrated by flight testing with an Osprey Aircraft. Prior to performing the experiment, the aircraft was modelled and the estimation method was tested in simulation. A Simulink modeling effort has been undertaken to develop a fully nonlinear, six degrees-of-freedom model of an Osprey aircraft. A simplified autopilot design is constructed, with inputs complementary with the outputs from the estimation method, and a specific maneuver is created to perform a simultaneous rolling, pitching, and yawing motion of the aircraft combined with a fixed mounted camera. The aircraft/autopilot modeling effort and maneuver is intended to test the robustness of the vision-based algorithm as well as to provide proof-of-concept in using the camera as the primary sensor for achieving closed-loop autonomous flight.

With the vehicle model as described, a baseline autopilot is incorporated to allow for the vehicle to perform simple commanded maneuvers that an autonomous aircraft would typically be expected to receive from an on-board guidance system. The autopilot architecture, given in Figure 3–2, is specifically designed to accept inputs compatible with the state estimates coming from the vision-based algorithms. Preliminary modal analysis of the Osprey vehicle flying at a 60 meter altitude at 25 meters/sec indicated a short-period frequency, $\omega_{sp} = 10.1$ rad/sec and damping, $\zeta_{sp} = 0.85$; a phugoid mode frequency, $\omega_{ph} = 0.34$ rad/sec and damping, $\zeta_{ph} = 0.24$; a dutch-roll frequency, $\omega_{dr} = 4.20$ rad/sec and damping, $\zeta_{dr} = 0.19$; a roll subsidence time constant of $\tau = 0.08$ sec.; and a spiral mode time-to-double, $ttd = 44.01$ sec. These values, which correspond to (2–13) and (2–14), are crucial for the auto-pilot design as well as in determining what, if any, of the state estimation values coming from the camera and proposed technique are favorable to

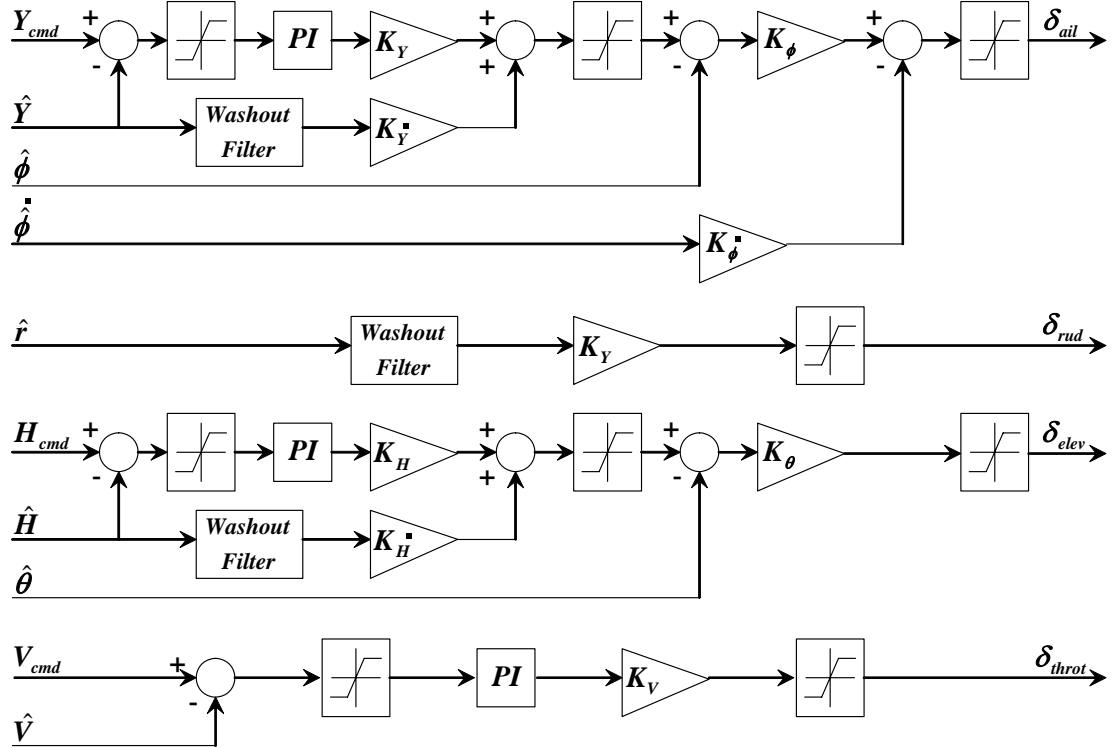


Figure 3–2: Rudimentary control system used for proof of concept for vision-based estimation algorithms.

be used in a closed-loop sense, as video frame rate and quantization noise become integral to the controller design from a frequency standpoint.

As the aircraft, with an integrated vision-based system, is required to fly in lesser benign regimes, such as maneuvering in and around structures, it becomes evident that simplistic classical control methods will be limited in performance capabilities. The aircraft system under consideration can be modeled via the following state space representation [2, 6, 11, 63, 64]:

$$\dot{x} = Ax + Bu + f(x, t) \quad (3-1)$$

$$y = Cx, \quad (3-2)$$

where $A \in \mathbb{R}^{n \times n}$ denotes the state matrix, $B \in \mathbb{R}^{n \times m}$ for $m < n$ represents the input matrix, $C \in \mathbb{R}^{m \times n}$ is the known output matrix, $u \in \mathbb{R}^m$ is a vector of control inputs, and $f(x, t) \in \mathbb{R}^n$ represents an unknown, nonlinear disturbance.

Assumption 1: The A and B matrices given in (3–1) contain parametric uncertainty.

Assumption 2: The nonlinear disturbance $f(x, t)$ and its first two time derivatives are assumed to exist and be bounded by a known constant.

3.3 Robust Control Development

In this section, it is described how a specific aircraft can be related to (3–1). Based on the standard assumption that the longitudinal and lateral modes of the aircraft are decoupled, the state space model for the Osprey aircraft testbed can be represented using (3–1) and (3–2), where the state matrix $A \in \mathbb{R}^{8 \times 8}$ and input matrix $B \in \mathbb{R}^{8 \times 4}$ given in chapter 2 are expressed as

$$A = \begin{bmatrix} A_{lon} & 0_{4 \times 4} \\ 0_{4 \times 4} & A_{lat} \end{bmatrix} \quad B = \begin{bmatrix} B_{lon} & 0_{4 \times 2} \\ 0_{4 \times 2} & B_{lat} \end{bmatrix}, \quad (3-3)$$

and the output matrix $C \in \mathbb{R}^{4 \times 8}$ is designed as

$$C = \begin{bmatrix} C_{lon} & 0_{2 \times 4} \\ 0_{2 \times 4} & C_{lat} \end{bmatrix}, \quad (3-4)$$

where $A_{lon}, A_{lat} \in \mathbb{R}^{4 \times 4}$, $B_{lon}, B_{lat} \in \mathbb{R}^{4 \times 2}$, and $C_{lon}, C_{lat} \in \mathbb{R}^{2 \times 4}$ denote the state matrices, input matrices, and output matrices, respectively, for the longitudinal and lateral subsystems, and the notation $0_{i \times j}$ denotes an $i \times j$ matrix of zeros. The state vector $x(t) \in \mathbb{R}^8$ is given as

$$x = \begin{bmatrix} x_{lon}^T & x_{lat}^T \end{bmatrix}^T, \quad (3-5)$$

where $x_{lon}(t), x_{lat}(t) \in \mathbb{R}^4$ denote the longitudinal and lateral state vectors defined as

$$x_{lon} \triangleq \begin{bmatrix} V & \alpha & q & \theta \end{bmatrix}^T \quad (3-6)$$

$$x_{lat} \triangleq \begin{bmatrix} \beta & p & r & \phi \end{bmatrix}^T, \quad (3-7)$$

where the state variables are defined as

$$V = \text{velocity} \quad \alpha = \text{angle of attack}$$

$$q = \text{pitch rate} \quad \theta = \text{pitch angle}$$

$$\beta = \text{sideslip angle} \quad p = \text{roll rate}$$

$$r = \text{yaw rate} \quad \phi = \text{bank angle}$$

and the control input vector is defined as

$$\begin{aligned} u &\triangleq \begin{bmatrix} u_{lon}^T & u_{lat}^T \end{bmatrix}^T \\ &= \begin{bmatrix} \delta_{elev} & \delta_{thrust} & \delta_{ail} & \delta_{rud} \end{bmatrix}^T. \end{aligned} \quad (3-8)$$

In (3-8), $\delta_{elev}(t) \in \mathbb{R}$ denotes the elevator deflection angle, $\delta_{thrust}(t) \in \mathbb{R}$ is the control thrust, $\delta_{ail}(t) \in \mathbb{R}$ is the aileron deflection angle, and $\delta_{rud}(t) \in \mathbb{R}$ is the rudder deflection angle.

The disturbance $f(x, t)$ introduced in (3-1) can represent several bounded nonlinearities. The more promising example of disturbances that can be represented by $f(x, t)$ is the nonlinear form of a selectively extracted portion of the state space matrix $A_{lon} \in \mathbb{R}^{4 \times 4}$ that would normally be linearized. This nonlinearity would then be added to the new state space plant by superposition, resulting in the following quasi-linear plant model:

$$\dot{x}_{lon} = A'_{lon}x_{lon} + B_{lon}u_{lon} + f(x_{lon}, t), \quad (3-9)$$

where $A'_{lon} \in \mathbb{R}^{4 \times 4}$ is the state space matrix A_{lon} with the linearized portion removed, and $f(x_{lon}, t) \in \mathbb{R}^4$ denotes the nonlinear disturbances present in the longitudinal dynamics. Some physical examples of $f(x_{lon}, t)$ would be the selective nonlinearities that cannot be ignored, such as when dealing with supermaneuvering vehicles, where post-stall angles of attack and inertia coupling, for example, are encountered. Given that the Osprey is a very benign maneuvering vehicle, $f(x, t)$ in this chapter will represent less rigorous nonlinearities for illustrative purposes. A similar technique can be followed with the lateral direction state space representation, where the nonlinear component of A_{lat} is extracted, and a new quasi-linear model for the lateral dynamics is developed as

$$\dot{x}_{lat} = A'_{lat}x_{lat} + B_{lat}u_{lat} + f(x_{lat}, t), \quad (3-10)$$

where $A'_{lat} \in \mathbb{R}^{4 \times 4}$ is the new lateral state matrix with the linearized components removed, and $f(x_{lat}, t) \in \mathbb{R}^4$ denotes the nonlinear disturbances present in the lateral dynamics. Another example of bounded nonlinear disturbances, which can be represented by $f(x, t)$ in (3-1), is a discrete vertical gust. The formula given in [65], for example, defines such a bounded nonlinearity in the longitudinal axis as

$$f_g(x_{lon}, t) = \begin{bmatrix} -11.1 \\ 7.2 \\ 37.4 \\ 0 \end{bmatrix} \frac{1}{V_0} \left\{ \frac{U_{ds}}{2} \left[1 - \cos\left(\frac{\pi s}{H}\right) \right] \right\}, \quad (3-11)$$

where H denotes the distance (between 10.67 and 106.68 meters) along the airplane's flight path for the gust to reach its peak velocity, V_0 is the forward velocity of the aircraft when it enters the gust, $s \in [0, 2H]$ represents the distance penetrated into the gust (e.g., $s = \int_{t_1}^{t_2} V(t) dt$), and U_{ds} is the design gust velocity as specified in [65]. This regulation is intended to be used to evaluate both vertical and lateral gust loads, so a similar representation can be developed for the lateral

dynamics. Another source of bounded nonlinear disturbances that could be represented by $f(x, t)$ is network delay from communication with a ground station.

3.4 Control Development

To facilitate the subsequent control design, a reference model can be developed as:

$$\dot{x}_m = A_m x_m + B_m \delta \quad (3-12)$$

$$y_m = C x_m, \quad (3-13)$$

with $A_m \in \mathbb{R}^{n \times n}$ and $B_m \in \mathbb{R}^{n \times m}$ designed as

$$A_m = \begin{bmatrix} A_{lonm} & 0_{4 \times 4} \\ 0_{4 \times 4} & A_{latm} \end{bmatrix} \quad B_m = \begin{bmatrix} B_{lonm} & 0_{4 \times 2} \\ 0_{4 \times 2} & B_{latm} \end{bmatrix}, \quad (3-14)$$

where A_m is Hurwitz, $\delta(t) \in \mathbb{R}^m$ is the reference input, $x_m \triangleq \begin{bmatrix} x_{lonm}^T & x_{latm}^T \end{bmatrix}^T \in \mathbb{R}^n$ represents the reference states, $y_m \in \mathbb{R}^m$ are the reference outputs, and C was defined in (3-2). The lateral and longitudinal reference models were chosen with the specific purpose of decoupling the longitudinal mode velocity and pitch rate as well as decoupling the lateral mode roll rate and yaw rate. In addition to this criterion, the design is intended to exhibit favorable transient response characteristics and to achieve zero steady-state error. Simultaneous and uncorrelated commands are input into each of the longitudinal and lateral model simulations to illustrate that each model indeed behaves as two completely decoupled second order systems.

The contribution in this control design is a robust technique to yield asymptotic tracking for an aircraft in the presence of parametric uncertainty in a non-square input authority matrix and an unknown nonlinear disturbance. To this end, the control law is developed based on the output dynamics, which enables us to transform the uncertain input matrix into a square matrix. By utilizing a

feedforward (best guess) estimate of the input uncertainty in the control law in conjunction with a robust control term, one is able to compensate for the input uncertainty. Specifically, based on the assumption that an estimate of the uncertain input matrix can be selected such that a diagonal dominance property is satisfied in the closed-loop error system, asymptotic tracking is proven.¹

3.4.1 Error System

The control objective is to ensure that the system outputs track desired time-varying reference outputs despite unknown, nonlinear, non-LP disturbances in the dynamic model. To quantify this objective, a tracking error, denoted by $e(t) \in \mathbb{R}^m$, is defined as

$$e = y - y_m = C(x - x_m). \quad (3-15)$$

To facilitate the subsequent analysis, a filtered tracking error [66], denoted by $r(t) \in \mathbb{R}^m$, is defined as:

$$r \triangleq \dot{e} + \alpha e, \quad (3-16)$$

where $\alpha \in \mathbb{R}^{m \times m}$ denotes a matrix of positive, constant control gains.

Remark 3.1: It can be shown that the system in (3-1) and (3-2) is bounded input bounded output (BIBO) stable in the sense that the unmeasurable states $x_u(t) \in \mathbb{R}^{n-m}$ and the corresponding time derivatives are bounded as

$$\|x_u\| \leq c_1 \|z\| + \zeta_{xu} \quad (3-17)$$

$$\|\dot{x}_u\| \leq c_2 \|z\| + \zeta_{\dot{x}_u}, \quad (3-18)$$

where $z(t) \in \mathbb{R}^{2m}$ is defined as

$$z \triangleq \begin{bmatrix} e^T & r^T \end{bmatrix}^T, \quad (3-19)$$

¹ Preliminary simulation results show that this assumption is mild in the sense that a wide range of estimates satisfy this requirement.

and $c_1, c_2, \zeta_{xu}, \zeta_{\dot{x}u} \in \mathbb{R}$ are known positive bounding constants, provided the control input $u(t)$ remains bounded during close-loop operation.

The open-loop tracking error dynamics can be developed by taking the time derivative of (3-16) and utilizing the expressions in (3-1), (3-2), (3-12), and (3-13) to obtain the following expression:

$$\dot{r} = \tilde{N} + N_d + \Omega(\dot{u} + \alpha u) - e, \quad (3-20)$$

where the auxiliary function $\tilde{N}(x, \dot{x}, e, \dot{e}) \in \mathbb{R}^m$ is defined as

$$\tilde{N} \triangleq CA(\dot{\underline{x}} - \dot{\underline{x}}_m) + \alpha CA(\underline{x} - \underline{x}_m) + CA(\dot{x}_{\rho u} + \alpha x_{\rho u}) + e \quad (3-21)$$

the auxiliary function $N_d(x_m, \dot{x}_m, \delta, \dot{\delta})$ is defined as

$$\begin{aligned} N_d = & CA(\dot{\underline{x}}_m + \alpha \underline{x}_m) + C\left(\dot{f}(x, t) + \alpha f(x, t)\right) - CA_m(\dot{x}_m + \alpha x_m) \\ & - CB_m(\dot{\delta} + \alpha \delta) + CA(\dot{x}_{\zeta u} + \alpha x_{\zeta u}), \end{aligned} \quad (3-22)$$

and the constant, unknown matrix $\Omega \in \mathbb{R}^{m \times m}$ is defined as

$$\Omega \triangleq CB. \quad (3-23)$$

In (3-21) and (3-22), $x_{\rho u}(t), \dot{x}_{\rho u}(t) \in \mathbb{R}^n$ contain the portions of $x_u(t)$ and $\dot{x}_u(t)$, respectively, that can be upper bounded by functions of the states, $x_{\zeta u}(t), \dot{x}_{\zeta u}(t) \in \mathbb{R}^n$ contain the portions of $x_u(t)$ and $\dot{x}_u(t)$ that can be upper bounded by known constants (i.e., see (3-17) and (3-18)), $\underline{x}(t) \in \mathbb{R}^n$ contains the measurable states (i.e., $x(t) = \underline{x}(t) + x_{\rho u}(t) + x_{\zeta u}(t)$), and $\underline{x}_m(t) \in \mathbb{R}^n$ contains the reference states corresponding to the measurable states $\underline{x}(t)$. The quantities $\tilde{N}(x, \dot{x}, e, \dot{e})$ and $N_d(x_m, \dot{x}_m, \delta, \dot{\delta})$ and the derivative $\dot{N}_d(x_m, \dot{x}_m, \ddot{x}_m, \delta, \dot{\delta}, \ddot{\delta})$ can be upper bounded

as follows:

$$\left\| \tilde{N} \right\| \leq \rho(\|z\|) \|z\| \quad (3-24)$$

$$\|N_d\| \leq \zeta_{N_d} \quad \left\| \dot{N}_d \right\| \leq \zeta_{\dot{N}_d}, \quad (3-25)$$

where $\zeta_{N_d}, \zeta_{\dot{N}_d} \in \mathbb{R}$ are known positive bounding constants, and the function $\rho(\|z\|)$ is a positive, globally invertible, nondecreasing function. Based on the expression in (3-20) and the subsequent stability analysis, the control input is designed as

$$\begin{aligned} u = & -\alpha \int_0^t u(\tau) d\tau - (k_s + 1) \hat{\Omega}^{-1} e(t) + (k_s + 1) \hat{\Omega}^{-1} e(0) - \int_0^t k_\gamma \hat{\Omega}^{-1} \text{sgn}(r(\tau)) d\tau \\ & - \hat{\Omega}^{-1} \int_0^t [(k_s + 1) \alpha e(\tau) + \beta \text{sgn}(e(\tau))] d\tau, \end{aligned} \quad (3-26)$$

where $\beta, k_s, k_\gamma \in \mathbb{R}^{m \times m}$ are diagonal matrices of positive, constant control gains, α was defined in (3-16), and the constant feedforward estimate $\hat{\Omega} \in \mathbb{R}^{m \times m}$ is defined as

$$\hat{\Omega} \triangleq C\hat{B}. \quad (3-27)$$

To simplify the notation in the subsequent stability analysis, the constant auxiliary matrix $\tilde{\Omega} \in \mathbb{R}^{m \times m}$ is defined as

$$\tilde{\Omega} \triangleq \Omega \hat{\Omega}^{-1}, \quad (3-28)$$

where $\tilde{\Omega}$ can be separated into diagonal and off-diagonal components as

$$\tilde{\Omega} = \Lambda + \Delta, \quad (3-29)$$

where $\Lambda \in \mathbb{R}^{m \times m}$ contains only the diagonal elements of $\tilde{\Omega}$, and $\Delta \in \mathbb{R}^{m \times m}$ contains the off-diagonal elements.

After substituting the time derivative of (3–26) into (3–20), the following closed-loop error system is obtained:

$$\begin{aligned} \dot{r} &= \tilde{N} + N_d - (k_s + 1)\tilde{\Omega}r - k_\gamma\tilde{\Omega}\text{sgn}(r) \\ &\quad - \tilde{\Omega}\beta\text{sgn}(e(t)) - e. \end{aligned} \quad (3-30)$$

Assumption 3: The constant estimate $\hat{\Omega}$ given in (3–27) is selected such that the following condition is satisfied:

$$\lambda_{\min}(\Lambda) - \|\Delta\| > \varepsilon, \quad (3-31)$$

where $\varepsilon \in \mathbb{R}$ is a known positive constant, and $\lambda_{\min}(\cdot)$ denotes the minimum eigenvalue of the argument. Preliminary testing results show this assumption is mild in the sense that (3–31) is satisfied for a wide range of $\hat{\Omega} \neq \Omega$.

Remark 3.2: A possible deficit of this control design is that the acceleration-dependent term $r(t)$ appears in the control input given in (3–26). This is undesirable from a controls standpoint; however, many aircraft controllers are designed based on the assumption that acceleration measurements are available [67–71]. Further, from (3–26), the sign of the acceleration is all that is required for measurement in this control design.

3.4.2 Stability Analysis

Theorem 3.1: The controller given in (3–26) ensures that the output tracking error is regulated in the sense that

$$\|e(t)\| \rightarrow 0 \quad \text{as } t \rightarrow \infty, \quad (3-32)$$

provided the control gain k_s introduced in (3–26) is selected sufficiently large (see the subsequent stability proof), and β and k_γ are selected according to the

following sufficient conditions:

$$\beta > \frac{(\zeta_{N_d} + \frac{1}{\alpha}\zeta_{\dot{N}_d})}{\lambda_{\min}(\Lambda)} \quad (3-33)$$

$$k_\gamma > \frac{\sqrt{m}\beta \|\Delta\|}{\varepsilon}, \quad (3-34)$$

where ζ_{N_d} and $\zeta_{\dot{N}_d}$ were introduced in (3-25), ε was defined in (3-31), and Λ and Δ were introduced in (3-29).

The following lemma is utilized in the proof of Theorem 3.1.

Lemma 3.1: Let $\mathcal{D} \subset \mathbb{R}^{2m+1}$ be a domain containing $w(t) = 0$, where $w(t) \in \mathbb{R}^{2m+1}$ is defined as

$$w(t) \triangleq \begin{bmatrix} z^T & \sqrt{P(t)} \end{bmatrix}^T, \quad (3-35)$$

and the auxiliary function $P(t) \in \mathbb{R}$ is defined as

$$\begin{aligned} P(t) \triangleq & \beta \|e(0)\| \|\Lambda\| - e(0)^T N_d(0) \\ & + \sqrt{m} \int_0^t \beta \|\Delta\| \|r(\tau)\| d\tau - \int_0^t L(\tau) d\tau. \end{aligned} \quad (3-36)$$

The auxiliary function $L(t) \in \mathbb{R}$ in (3-36) is defined as

$$L(t) \triangleq r^T \left(N_d(t) - \beta \tilde{\Omega} \text{sgn}(e) \right). \quad (3-37)$$

Provided the sufficient conditions in (3-33) is satisfied, the following inequality can be obtained:

$$\begin{aligned} \int_0^t L(\tau) d\tau \leq & \beta \|e(0)\| \|\Lambda\| - e(0)^T N_d(0) \\ & + \sqrt{m} \int_0^t \beta \|\Delta\| \|r(\tau)\| d\tau. \end{aligned} \quad (3-38)$$

Hence, (3-38) can be used to conclude that $P(t) \geq 0$.

Proof: (See Theorem 1) Let $V(w, t) : \mathcal{D} \times [0, \infty) \rightarrow \mathbb{R}$ be a continuously differentiable, positive definite function defined as

$$V \triangleq \frac{1}{2}e^T e + \frac{1}{2}r^T r + P, \quad (3-39)$$

where $e(t)$ and $r(t)$ are defined in (5-11) and (3-16), respectively, and the positive definite function $P(t)$ is defined in (3-36). The positive definite function $V(w, t)$ satisfies the inequality

$$U_1(w) \leq V(w, t) \leq U_2(w), \quad (3-40)$$

provided the sufficient condition introduced in (3-33) is satisfied. In (3-40), the continuous, positive definite functions $U_1(w), U_2(w) \in \mathbb{R}$ are defined as

$$U_1 \triangleq \frac{1}{2} \|w\|^2 \quad U_2 \triangleq \|w\|^2. \quad (3-41)$$

After taking the derivative of (3-39) and utilizing (3-16), (3-29), (3-30), (3-36), and (3-37), $\dot{V}(w, t)$ can be expressed as

$$\begin{aligned} \dot{V}(w, t) = & -\alpha e^T e + r^T \tilde{N} - (k_s + 1) r^T \Lambda r \\ & - (k_s + 1) r^T \Delta r + \sqrt{m} \beta \|r\| \|\Delta\| \\ & - k_\gamma r^T \Delta \operatorname{sgn}(r) - k_\gamma r^T \Lambda \operatorname{sgn}(r). \end{aligned} \quad (3-42)$$

By utilizing (3-24), $\dot{V}(w, t)$ can be upper bounded as

$$\begin{aligned} \dot{V}(w, t) \leq & -\alpha e^T e - \varepsilon \|r\|^2 - k_s \varepsilon \|r\|^2 \\ & + \rho(\|z\|) \|r\| \|z\| + [-k_\gamma \varepsilon + \sqrt{m} \beta \|\Delta\|] \|r\|. \end{aligned} \quad (3-43)$$

Clearly, if (3-34) is satisfied, the bracketed term in (3-43) is negative, and $\dot{V}(w, t)$ can be upper bounded using the squares of the components of $z(t)$ as follows:

$$\begin{aligned} \dot{V}(w, t) \leq & -\alpha \|e\|^2 - \varepsilon \|r\|^2 \\ & + [\rho(\|z\|) \|r\| \|z\| - k_s \varepsilon \|r\|^2]. \end{aligned} \quad (3-44)$$

Completing the squares for the bracketed terms in (3-44) yields

$$\dot{V}(w, t) \leq -\eta_3 \|z\|^2 + \frac{\rho^2 (\|z\|) \|z\|^2}{4k_s \varepsilon}, \quad (3-45)$$

where $\eta_3 \triangleq \min \{\alpha, \varepsilon\}$, and $\rho(\|z\|)$ is introduced in (3-24). The following expression can be obtained from (3-45):

$$\dot{V}(w, t) \leq -U(w), \quad (3-46)$$

where $U(w) = c \|z\|^2$, for some positive constant $c \in \mathbb{R}$, is a continuous, positive semi-definite function that is defined on the following domain:

$$\mathcal{D} \triangleq \left\{ w \in \mathbb{R}^{2m+1} \mid \|w\| < \rho^{-1} \left(2\sqrt{\eta_3 k_s \varepsilon} \right) \right\}. \quad (3-47)$$

The inequalities in (3-40) and (3-46) can be used to show that $V(t) \in \mathcal{L}_\infty$ in \mathcal{D} ; hence $e(t), r(t) \in \mathcal{L}_\infty$ in \mathcal{D} . Given that $e(t), r(t) \in \mathcal{L}_\infty$ in \mathcal{D} , standard linear analysis methods can be used to prove that $\dot{e}(t) \in \mathcal{L}_\infty$ in \mathcal{D} from (3-16). Since $e(t), \dot{e}(t) \in \mathcal{L}_\infty$ in \mathcal{D} , the assumption that $y_m, \dot{y}_m \in \mathcal{L}_\infty$ in \mathcal{D} can be used along with (5-11) to prove that $y, \dot{y} \in \mathcal{L}_\infty$ in \mathcal{D} . Given that $r(t) \in \mathcal{L}_\infty$ in \mathcal{D} , the assumption that $\hat{\Omega}^{-1} \in \mathcal{L}_\infty$ in \mathcal{D} can be used along with the time derivative of (3-26) to show that $\dot{u}(t) \in \mathcal{L}_\infty$ in \mathcal{D} . Further, Equation 2.78 of [72] can be used to show that $\dot{u}(t)$ can be upper bounded as $\dot{u}(t) \leq -\alpha u(\tau) + M, \forall t \geq 0$, where $M \in \mathbb{R}^+$ is a bounding constant. Theorem 1.1 of [73] can then be utilized to show that $u(t) \in \mathcal{L}_\infty$ in \mathcal{D} . Hence, (3-30) can be used to show that $\dot{r}(t) \in \mathcal{L}_\infty$ in \mathcal{D} . Since $\dot{e}(t), \dot{r}(t) \in \mathcal{L}_\infty$ in \mathcal{D} , the definitions for $U(w)$ and $z(t)$ can be used to prove that $U(w)$ is uniformly continuous in \mathcal{D} . Let $S \subset \mathcal{D}$ denote a set defined as follows:

$$S \triangleq \left\{ w(t) \in \mathcal{D} \mid U_2(w(t)) < \frac{1}{2} \left(\rho^{-1} \left(2\sqrt{\varepsilon \eta_3 k_s} \right) \right)^2 \right\}. \quad (3-48)$$

Theorem 8.4 of [74] can now be invoked to state that

$$c \|z\|^2 \rightarrow 0 \quad \text{as} \quad t \rightarrow \infty \quad \forall w(0) \in S. \quad (3-49)$$

Based on the definition of z , (3-49) can be used to show that

$$\|e(t)\| \rightarrow 0 \quad \text{as} \quad t \rightarrow \infty \quad \forall w(0) \in S. \quad (3-50)$$

3.5 Simulation Results

A numerical simulation was created to test the efficacy of the proposed controller. The simulation is based on the aircraft state space system given in (3-1) and (3-2), where the state matrix A , input authority matrix B , and nonlinear disturbance function $f(x)$ are given by the state space model for the Osprey aircraft given in (3-3)-(3-8). The reference model for the simulation is represented by the state space system given in (3-12)-(3-14), with state matrices A_{lonm} and A_{latm} , input matrices B_{lonm} and B_{latm} , and output matrices C_{lon} and C_{lat} selected as

$$A_{lonm} = \begin{bmatrix} 0.6 & -1.1 & 0 & 0 \\ 2.0 & -2.2 & 0 & 0 \\ 0 & 0 & -4.0 & -600.0 \\ 0 & 0 & 0.1 & -10 \end{bmatrix} \quad (3-51)$$

$$A_{latm} = \begin{bmatrix} -4.0 & -600.0 & 0 & 0 \\ 0.1 & -10.00 & 0 & 0 \\ 0 & 0 & 0.6 & -1.1 \\ 0 & 0 & 2.0 & -2.2 \end{bmatrix} \quad (3-52)$$

$$B_{lonm} = \begin{bmatrix} 0 & 0.5 \\ 0 & 0 \\ 10 & 0 \\ 0 & 0 \end{bmatrix} \quad B_{latm} = \begin{bmatrix} 10 & 0 \\ 0 & 0 \\ 0 & 0.5 \\ 0 & 0 \end{bmatrix}, \quad (3-53)$$

and

$$C_{lon} = \begin{bmatrix} 0 & 0 & 1 & 0 \\ 1 & 0 & 0 & 0 \end{bmatrix} \quad C_{lat} = \begin{bmatrix} 0 & 1 & 0 & 0 \\ 0 & 0 & 1 & 0 \end{bmatrix}. \quad (3-54)$$

The longitudinal and lateral dynamic models for the Osprey aircraft flying at 25 m/s at an altitude of 60 meters are represented using (3-9) and (3-10), where A'_{lon} , A'_{lat} , B_{lon} , and B_{lat} are given as

$$A'_{lon} = \begin{bmatrix} -0.15 & 11.08 & 0.08 & 0 \\ -0.03 & -7.17 & 0.83 & 0 \\ 0 & -37.35 & -9.96 & 0 \\ 0 & 0 & 1.00 & 0 \end{bmatrix} \quad (3-55)$$

$$A'_{lat} = \begin{bmatrix} -0.69 & -0.03 & -0.99 & 0 \\ -3.13 & -12.92 & 1.10 & 0 \\ 17.03 & -0.10 & -0.97 & 0 \\ 0 & 1.00 & -0.03 & 0 \end{bmatrix} \quad (3-56)$$

$$B_{lon} = \begin{bmatrix} 3E^{-3} & 0.06 \\ 1E^{-5} & 1E^{-4} \\ 0.98 & 0 \\ 0 & 0 \end{bmatrix} \quad B_{lat} = \begin{bmatrix} 0 & 0 \\ 1.50 & -0.02 \\ -0.09 & 0.17 \\ 0 & 0 \end{bmatrix}, \quad (3-57)$$

respectively. The nonlinear disturbance terms $f(x_{lon}, t)$ and $f(x_{lat}, t)$ introduced in (3-9) and (3-10), respectively, are defined as

$$f(x_{lon}, t) = \begin{bmatrix} -9.81 \sin \theta & 0 & 0 & 0 \end{bmatrix}^T + f_g(x_{lon}, t) \quad (3-58)$$

$$f(x_{lat}, t) = \begin{bmatrix} 0.39 \sin \phi & 0 & 0 & 0 \end{bmatrix}^T, \quad (3-59)$$

where $f_g(x_{lon}, t)$ represents a disturbance due to a discrete vertical wind gust as defined in (3-11), where $U_{ds} = 10.12 \text{ m/s}$, $H = 15.24 \text{ m}$, and $V_0 = 25$

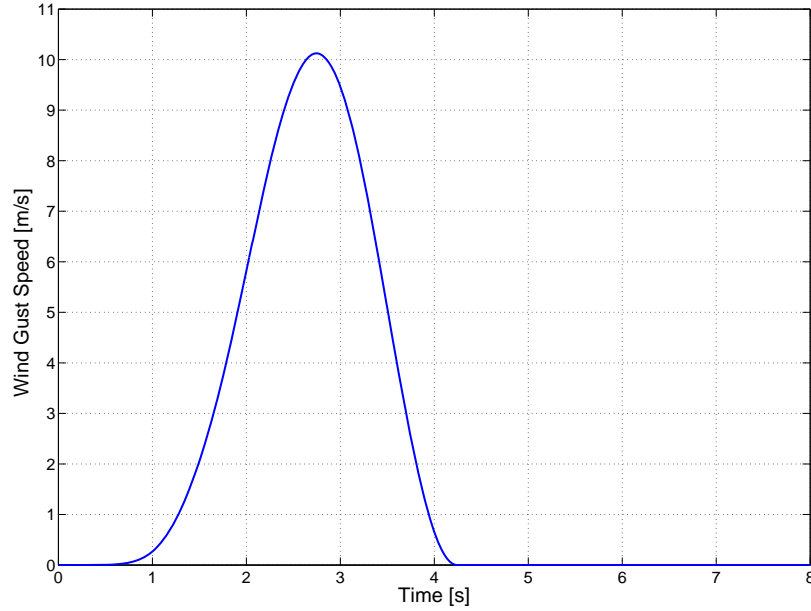


Figure 3–3: Plot of the discrete vertical (upward) wind gust used in the controller simulation.

m/s (cruise velocity). Figure 3–3 shows a plot of the wind gust used in the simulation. The remainder of the additive disturbances in (3–58) and (3–59) represent nonlinearities not captured in the linearized state space model (e.g., due to small angle assumptions). All states and control inputs were initialized to zero for the simulation.

The feedforward estimates \hat{B}_{lon} and \hat{B}_{lat} were selected as

$$\hat{B}_{lon} = \begin{bmatrix} 0.01 & 0.1 \\ 0 & 0 \\ 1.4 & 0 \\ 0 & 0 \end{bmatrix} \quad \hat{B}_{lat} = \begin{bmatrix} 0 & 0 \\ 1.7 & -0.05 \\ -0.1 & 0.25 \\ 0 & 0 \end{bmatrix}. \quad (3-60)$$

Remark 3.3: For the choices for \hat{B}_{lon} and \hat{B}_{lat} given in (3–60), the inequality in (3–31) is satisfied. Specifically, the choice for \hat{B}_{lon} yields the following:

$$\lambda_{\min}(\Lambda) = 0.6450 > 0.0046 = \|\Delta\|, \quad (3-61)$$

Table 3–1: Parameters used in the controller simulation.

Sampling Time	0.01 sec
Pitch Rate Sensor Noise	$\pm 1.7^\circ / \text{sec}$
Velocity Sensor Noise	$\pm 0.4 \text{ m} / \text{sec}$
Roll Rate Sensor Noise	$\pm 1.7^\circ / \text{sec}$
Yaw Rate Sensor Noise	$\pm 1.7^\circ / \text{sec}$
Control Thrust Saturation Limit	$\pm 200 \text{ N}$
Control Thrust Rate Limit	$\pm 200 \text{ N} / \text{sec}$
Elevator Saturation Limit	$\pm 30^\circ$
Elevator Rate Limit	$\pm 300^\circ / \text{sec}$
Aileron Saturation Limit	$\pm 30^\circ$
Aileron Rate Limit	$\pm 300^\circ / \text{sec}$
Rudder Saturation Limit	$\pm 30^\circ$
Rudder Rate Limit	$\pm 300^\circ / \text{sec}$

and the choice for \hat{B}_{lat} yields

$$\lambda_{\min}(\Lambda) = 0.6828 > 0.0842 = \|\Delta\|. \quad (3-62)$$

In order to develop a realistic stepping stone to an actual experimental demonstration of the proposed aircraft controller, the simulation parameters were selected based on detailed data analyses and specifications. The sensor noise values are based upon Cloud Cap Technology’s Piccolo Autopilot and analysis of data logged during straight and level flight. These values are also corroborated with the specifications given for Cloud Cap Technology’s Crista Inertial Measurement Unit (IMU). The thrust limit and estimated rate limit was measured via a static test using a fish scale. The control surface rate and position limits were determined via the geometry of the control surface linkages in conjunction with the detailed specifications sheet given with the Futaba S3010 standard ball bearing servo. The simulation parameters are summarized in Table 1.

The objectives for the longitudinal controller simulation are to track pitch rate and forward velocity commands. Figure 3–4 shows the simulation results of

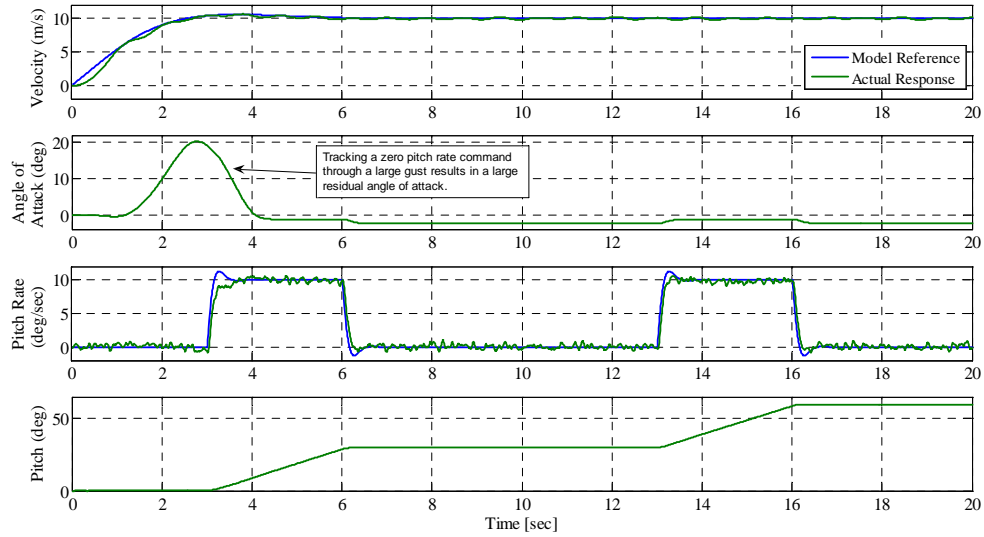


Figure 3–4: Illustration of uncoupled velocity and pitch rate response during closed-loop longitudinal controller operation.

the closed-loop longitudinal system with control gains selected as follows (e.g., see (3–23) and (3–26))² :

$$\beta = \text{diag} \left\{ \begin{array}{cc} 0.1 & 130 \end{array} \right\} \quad k_s = \text{diag} \left\{ \begin{array}{cc} 0.2 & 160 \end{array} \right\}$$

$$\alpha = \text{diag} \left\{ \begin{array}{cc} 0.7 & 0.1 \end{array} \right\} \quad k_\gamma = 0.1I_{2 \times 2},$$

where the notation $I_{j \times j}$ denotes the $j \times j$ identity matrix. Figure 3–4 shows the actual responses versus the reference commands for velocity and pitch rate. Note that the uncontrolled states remain bounded. For the lateral controller simulation, the objectives are to track roll rate and yaw rate commands. Figure 3–5 shows the simulation results of the closed-loop lateral system with control gains selected as

² The k_γ used in the longitudinal controller simulation does not satisfy the sufficient condition given in (3–34); however, this condition is not necessary for stability, it is sufficient for the Lyapunov stability proof.

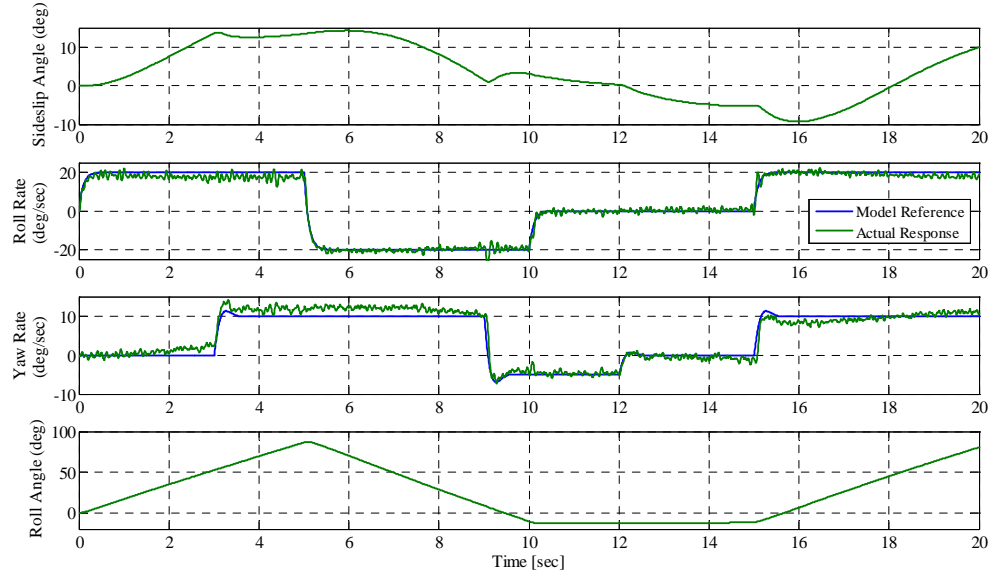


Figure 3–5: Illustration of uncoupled roll rate and yaw rate response during closed-loop lateral controller operation.

follows:

$$\beta = \text{diag} \left\{ \begin{array}{cc} 0.2 & 0.6 \end{array} \right\} \quad k_s = \text{diag} \left\{ \begin{array}{cc} 0.2 & 3 \end{array} \right\}$$

$$\alpha = \text{diag} \left\{ \begin{array}{cc} 1.0 & 0.2 \end{array} \right\} \quad k_\gamma = I_{2 \times 2}.$$

Figure 3–5 shows the actual responses versus the reference commands for roll rate and yaw rate. Note that the uncontrolled states remain bounded.

3.6 Conclusion

An aircraft controller is presented, which achieves asymptotic tracking control of a model reference system where the plant dynamics contain input uncertainty and a bounded non-LP disturbance. The developed controller exhibits the desirable characteristic of tracking the specified decoupled reference model. An example of such a decoupling is demonstrated by examining the aircraft response to tracking a roll rate command while simultaneously tracking a completely unrelated yaw rate command. This result represents the first ever application of a continuous

control strategy in a DI and MRAC framework to a nonlinear system with additive, non-LP disturbances, where the control input is multiplied by a non-square matrix containing parametric uncertainty. To achieve the result, a novel robust control technique is combined with a RISE control structure. A Lyapunov-based stability analysis is provided to verify the theoretical result, and simulation results demonstrate the robustness of the controller to sensor noise, exogenous perturbations, parametric uncertainty, and plant nonlinearities, while simultaneously exhibiting the capability to emulate a reference model designed offline. Future efforts will focus on eliminating the acceleration-dependent term from the control input and designing adaptive feedforward estimates of the uncertainties.

CHAPTER 4 DAISY-CHAINING FOR STATE ESTIMATION

4.1 Introduction

While a Global Positioning System (GPS) is the most widely used sensor modality for aircraft navigation, researchers have been motivated to investigate other navigational sensor modalities because of the desire to operate in GPS denied environments. Due to advances in computer vision and control theory, monocular camera systems have received growing interest as an alternative/collaborative sensor to GPS systems. Cameras can act as navigational sensors by detecting and tracking feature points in an image. Current methods have a limited ability to relate feature points as they enter and leave the camera field of view.

This chapter details a vision-based position and orientation estimation method for aircraft navigation and control. This estimation method accounts for a limited camera field of view by releasing tracked features that are about to leave the field of view and tracking new features. At each time instant that new features are selected for tracking, the previous pose estimate is updated. The vision-based estimation scheme can provide input directly to the vehicle guidance system and autopilot. Simulations are performed wherein the vision-based pose estimation is integrated with a new, nonlinear flight model of an aircraft. Experimental verification of the pose estimation is performed using the modelled aircraft.

The efforts in this chapter (and our preliminary results [76, 77]) explore the use of a single camera as a sole sensor to estimate the position and orientation of an aircraft through use of the Euclidean Homography. The method is designed for use with a fixed wing aircraft, thus the method explicitly acquires new feature points when the current features risk leaving the image, and no target model is needed,

as compared to other methods [31]- [40]. The contribution of this chapter is the use of homographic relationships that are linked in a unique way through a novel “daisy-chaining” method.

4.2 Pose Reconstruction From Two Views

4.2.1 Euclidean Relationships

Consider a body-fixed coordinate frame \mathcal{F}_c that defines the position and attitude of a camera with respect to a constant world frame \mathcal{F}_w . The world frame could represent a departure point, destination, or some other point of interest. The rotation and translation of \mathcal{F}_c with respect to \mathcal{F}_w is defined as $R(t) \in \mathbb{R}^{3 \times 3}$ and $x(t) \in \mathbb{R}^3$, respectively. The camera rotation and translation from $\mathcal{F}_c(t_0)$ to $\mathcal{F}_c(t_1)$ between two sequential time instances, t_0 and t_1 , is denoted by $R_{01}(t_1)$ and $x_{01}(t_1)$. During the camera motion, a collection of I (where $I \geq 4$) coplanar and non-collinear static feature points are assumed to be visible in a plane π . The assumption of four coplanar and non-collinear feature points is only required to simplify the subsequent analysis and is made without loss of generality. Image processing techniques can be used to select coplanar and non-collinear feature points within an image. However, if four coplanar target points are not available then the subsequent development can also exploit a variety of linear solutions for eight or more non-coplanar points (e.g., the classic eight points algorithm [78, 79]), or nonlinear solutions for five or more points [80].

A feature point $p_i(t)$ has coordinates $\bar{m}_i(t) = [x_i(t), y_i(t), z_i(t)]^T \in \mathbb{R}^3 \forall i \in \{1 \dots I\}$ in \mathcal{F}_c . Standard geometric relationships can be applied to the coordinate systems depicted in Figure 4-1 to develop the following relationships:

$$\begin{aligned} \bar{m}_i(t_1) &= R_{01}(t_1)\bar{m}_i(t_0) + x_{01}(t_1) \\ \bar{m}_i(t_1) &= \underbrace{\left(R_{01}(t_1) + \frac{x_{01}(t_1)}{d(t_0)}n(t_0)^T \right)}_{H(t_1)} \bar{m}_i(t_0) \end{aligned} \quad (4-1)$$

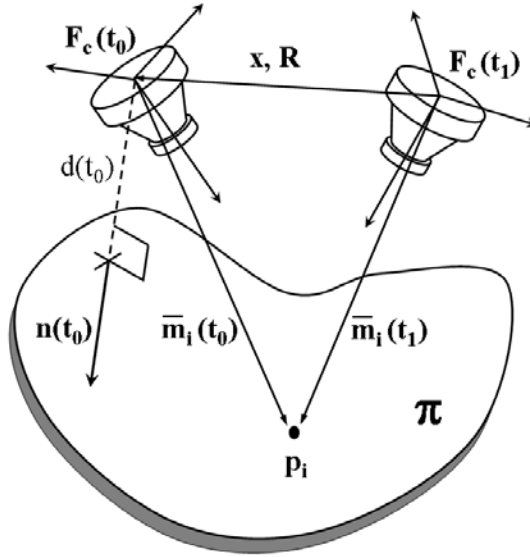


Figure 4-1: Euclidean relationships between two camera poses.

where $H(t)$ is the Euclidean Homography matrix, and $n(t_0)$ is the constant unit vector normal to the plane π from $\mathcal{F}_c(t_0)$, and $d(t_0)$ is the constant distance between the plane π and $\mathcal{F}_c(t_0)$ along $n(t_0)$. After normalizing the Euclidean coordinates as

$$m_i(t) = \frac{\bar{m}_i(t)}{z_i(t)} \quad (4-2)$$

the relationship in (4-1) can be rewritten as

$$m_i(t_1) = \underbrace{\frac{z_i(t_0)}{z_i(t_1)}}_{\alpha_i} H m_i(t_0) \quad (4-3)$$

where $\alpha_i \in \mathbb{R} \forall i \in \{1 \dots I\}$ is a scaling factor.

4.2.2 Projective Relationships

Using standard projective geometry, the Euclidean coordinate $\bar{m}_i(t)$ can be expressed in image-space pixel coordinates as $p_i(t) = [u_i(t), v_i(t), 1]^T$. The projected pixel coordinates are related to the normalized Euclidean coordinates, $m_i(t)$ by the pin-hole camera model as [81]

$$p_i = A m_i, \quad (4-4)$$

where A is an invertible, upper triangular camera calibration matrix defined as

$$A \triangleq \begin{bmatrix} a & -a \cos \phi & u_0 \\ 0 & \frac{b}{\sin \phi} & v_0 \\ 0 & 0 & 1 \end{bmatrix}. \quad (4-5)$$

In (4-5), u_0 and $v_0 \in \mathbb{R}$ denote the pixel coordinates of the principal point (the image center as defined by the intersection of the optical axis with the image plane), $a, b \in \mathbb{R}$ represent scaling factors of the pixel dimensions, and $\phi \in \mathbb{R}$ is the skew angle between camera axes.

By using (4-4), the Euclidean relationship in (4-3) can be expressed as

$$p_i(t_1) = \alpha_i A H A^{-1} p_i(t_0) = \alpha_i G p_i(t_0). \quad (4-6)$$

Sets of linear equations can be developed from (4-6) to determine the projective and Euclidean Homography matrices $G(t)$ and $H(t)$ up to a scalar multiple.

Given images of four or more feature points taken at $\mathcal{F}_c(t_0)$ and $\mathcal{F}_c(t_1)$, various techniques [82, 83] can be used to decompose the Euclidean Homography to obtain $\alpha_i(t_1)$, $n(t_0)$, $\frac{x_{01}(t_1)}{d(t_0)}$ and $R_{01}(t_1)$. The distance $d(t_0)$ must be separately measured (e.g., through an altimeter or radar range finder) or estimated using a priori knowledge of the relative feature point locations, stereoscopic cameras, or as an estimator signal in a feedback control.

4.2.3 Chained Pose Reconstruction for Aerial Vehicles

Consider an aerial vehicle equipped with a GPS and a camera capable of viewing a landscape. A technique is developed in this section to estimate the position and attitude using camera data when the GPS signal is denied. A camera has a limited field of view, and motion of a vehicle can cause observed feature points to leave the image. The method presented here chains together pose estimations from sequential sets of tracked of points. This approach allows the system to halt tracking a set of image features if it is likely to leave the image and

begin tracking a new set of features while maintaining the pose estimate. Thus, the estimation can continue indefinitely and is not limited by the camera's field of view.

The subsequent development assumes that the aerial vehicle begins operating in a GPS denied environment at time t_0 , where the translation and rotation (i.e., $R_o(t_0)$ and $x_0(t_0)$ in Figure 4-2) between $\mathcal{F}_c(t_0)$ and $\mathcal{F}_w(t_0)$ is known. The rotation between $\mathcal{F}_c(t_0)$ and $\mathcal{F}_w(t_0)$ can be determined through the bearing information of the GPS along with other sensors such as a gyroscope and/or compass. Without loss of generality, the GPS unit is assumed to be fixed to the origin of the aerial vehicle's coordinate frame, and the constant position and attitude of the camera frame is known with respect to the position and attitude of the aerial vehicle coordinate frame. The subsequent development further assumes that the GPS is capable of delivering altitude, perhaps in conjunction with an altimeter, so that the altitude $a(t_0)$ is known.

As illustrated in Figure 4-2, the initial set of tracked coplanar and non-coplanar feature points are contained in the plane π_a . These feature points have Euclidean coordinates $\bar{m}_{ai}(t_0) \in \mathbb{R}^3 \forall i \in \{1 \dots I\}$ in \mathcal{F}_c . The plane π_a is perpendicular to the unit vector $n_a(t_0)$ in the camera frame, and lies at a distance $d_a(t_0)$ from the camera frame origin. At time t_1 , the vehicle has some rotation $R_{01}(t_1)$ and translation $x_{01}(t_1)$ that can be determined from the images by decomposing the relationships given in (4-6). For notational simplicity, the subscript i is omitted in subsequent development.

As described earlier, $R_{01}(t_1)$ and $\frac{x_{01}(t_1)}{d_a(t_0)}$ can be solved from two corresponding images of the feature points $p_a(t_0)$ and $p_a(t_1)$. A measurement or estimate for $d_a(t_0)$ is required to recover $x_{01}(t_1)$. This estimation is possible with distance sensors or with a priori knowledge of the geometric distances between the points in π_a . However, with an additional assumption, it is possible to estimate $d_a(t_0)$ geometrically using altitude information from the last GPS reading and/or an

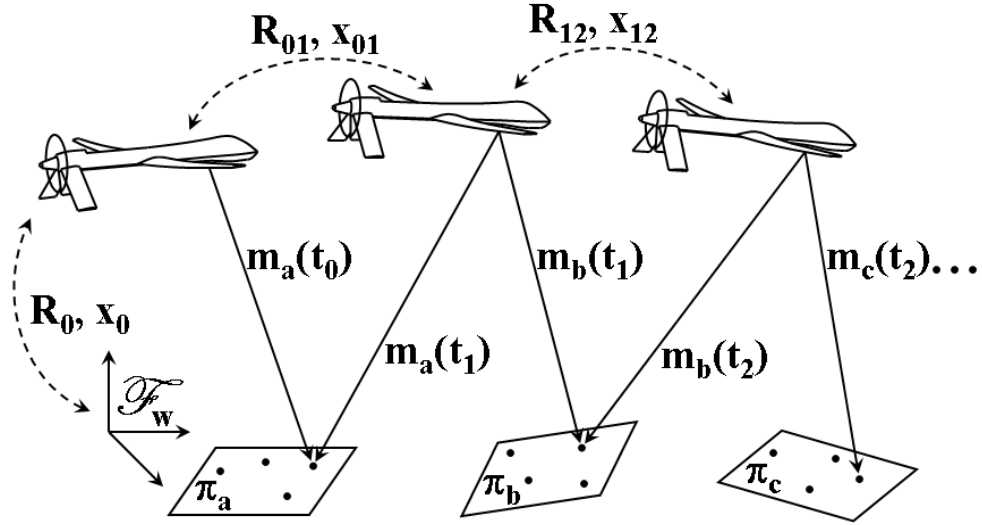


Figure 4-2: Illustration of pose estimation chaining.

altimeter. From the illustration in Figure 4-3, if $a(t_0)$ is the height above π_a (e.g., the slope of the ground is constant between the feature points and projection of the plane's location to the ground), then the distance $d_a(t_0)$ can be determined as

$$d_a(t_0) = n_a(t_0) \cdot a(t_0). \quad (4-7)$$

where $n_a(t_0)$ is known from the homography decomposition.

Once $R_{01}(t_1)$, $d_a(t_0)$, and $x_{01}(t_1)$ have been determined, the rotation $R_1(t_1)$ and translation $x_1(t_1)$ can be determined with respect to \mathcal{F}_w as

$$R_1 = R_0 R_{01}$$

$$x_1 = R_{01} x_{01} + x_0.$$

As illustrated in Figure 4-2, a new collection of feature points $p_b(t)$ can be obtained that correspond to a collection of points on a planar patch denoted by π_b . At time t_2 , the sets of points $p_b(t_1)$ and $p_b(t_2)$ can be used to determine $R_{12}(t_2)$ and $\frac{x_{12}(t_2)}{d_b(t_1)}$, which provides the rotation and scaled translation of \mathcal{F}_c with respect to \mathcal{F}_w . If π_b

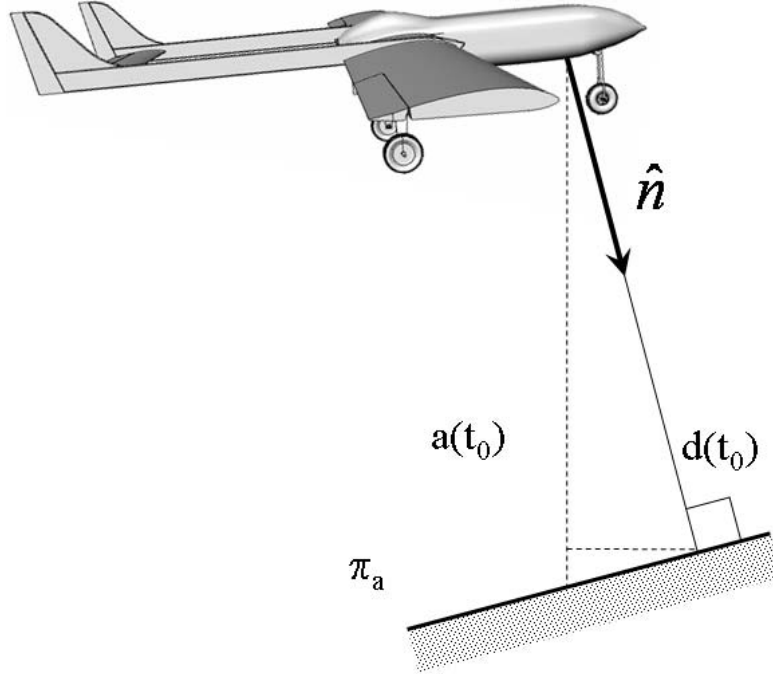


Figure 4–3: Depth estimation from altitude.

and π_a are the same plane, then $d_b(t_1)$ can be determined as

$$d_b(t_1) = d_a(t_1) = d_a(t_0) + x_{01}(t_1) \cdot n(t_0). \quad (4-8)$$

When π_b and π_a are the same plane $x_{12}(t_2)$ can be correctly scaled, and $R_2(t_2)$ and $x_2(t_2)$ can be computed in a similar manner as described for $R_1(t_1)$ and $x_1(t_1)$.

Estimations can be propagated by chaining them together at each time instance without further use of GPS.

In the general case, p_b and p_a are not coplanar and (4–8) cannot be used to determine $d_b(t_1)$. If p_b and p_a are both visible for two or more frames, it is still possible to calculate $d_b(t)$ through geometric means. Let t_{1-} denote as some time before the daisy chain operation is performed, when both p_b and p_a are visible in the image. At time t_{1-} , an additional set of homography equations for the points p_b and p_a at times t_1 and t_{1-} can be solved for

$$m_{ai}(t_1) = \alpha_a \left(R + \frac{xn_a(t_{1-})^T}{d_a(t_{1-})} \right) m_{ai}(t_{1-}) \quad (4-9)$$

$$m_{bi}(t_1) = \alpha_b \left(R + \frac{xn_b(t_{1-})^T}{d_b(t_{1-})} \right) m_{bi}(t_{1-}) \quad (4-10)$$

where $\alpha_a = \frac{z_{ai}(t_{1-})}{z_{ai}(t)}$ and $\alpha_b = \frac{z_{bi}(t_{1-})}{z_{bi}(t)}$.

Note that $R(t_1)$ and $x(t_1)$ have the same values in equations (4-9) and (4-10), but the distance and normal to the plane are different for the two sets of points. The distance $d_a(t_{1-})$ is known from using (4-8). Define $x_b(t_1) = \frac{x(t_1)}{d_b(t_{1-})}$ and $x_a(t_1) = \frac{x(t_1)}{d_a(t_{1-})}$. The translation $x(t_1)$ is solved as

$$x = d_a(t_{1-})x_a,$$

and then determining $d_b(t_{1-})$

$$d_b(t_{1-}) = \frac{x_b^T x}{\|x_b\|}.$$

$d_b(t_1)$ can then be found by using (4-8) with $d_b(t_{1-})$ in place of $d_a(t_0)$. Additional sensors, such as an altimeter, can provide an additional estimate in the change in altitude. These estimates can be used in conjunction with (4-8) to update depth estimates.

Image-Based Rate Gyro.

Additional uses are found from the homography decomposition that can be used for feedback control. As an example, Poisson's kinematic differential equation for the direction cosine matrix, R states

$$\dot{R} = - \begin{bmatrix} 0 & -r & q \\ r & 0 & -p \\ -q & p & 0 \end{bmatrix} R,$$

which can also be expressed as

$$\begin{bmatrix} 0 & -r & q \\ r & 0 & -p \\ -q & p & 0 \end{bmatrix} = -\dot{R}R^T.$$

Hence, aircraft body rates, $p(t)$, $q(t)$, and $r(t)$ can be estimated via $R(t)$ from the homography decomposition along with the time derivative of $R(t)$.

4.2.4 Simulation Results

In the simulations, five patches of 4 feature points are manually placed along a 500 meter ground track, which the vehicle flies over. For simplicity, all planar patches lie in the same plane. The task is to perform the state estimation during a maneuver. The commanded maneuver is to simultaneously perform a 10 meter lateral shift to the right and a 10 meter longitudinal increase in altitude. This particular maneuver results in the vehicle simultaneously pitching, rolling, and yawing, while translating. For simulation purposes, the camera is mounted underneath the fuselage looking downwards. The camera model for this exercise is intended to be representative of a typical 640×480 lines of resolution CCD camera equipped with a 10 mm lens. To more accurately capture true system performance, pixel coordinates were rounded to the nearest integer to model errors due to camera pixilation effects (i.e. quantization noise), furthermore a 5% error was added to the estimated vehicle altitude to test robustness.

The first simulation was designed to test the accuracy of the vision-based estimation. Vision was not used in the feedback in this maneuver, and the estimated pose is compared to the true pose. The results of this preliminary analysis are given in Figures 4-4 and 4-5. The effects of noise are visible but the estimated pose is accurate.

The second simulation was intended to examine the effects of using the vision based estimate as a sensor in closed-loop control. This simulation involved

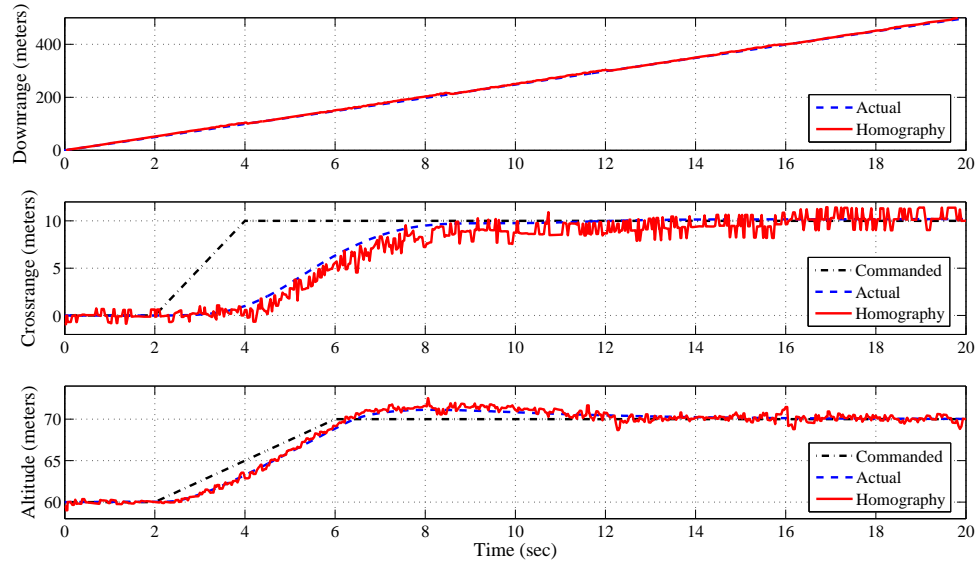


Figure 4–4: Actual translation versus estimated translation where the estimation is not part of the closed-loop control.

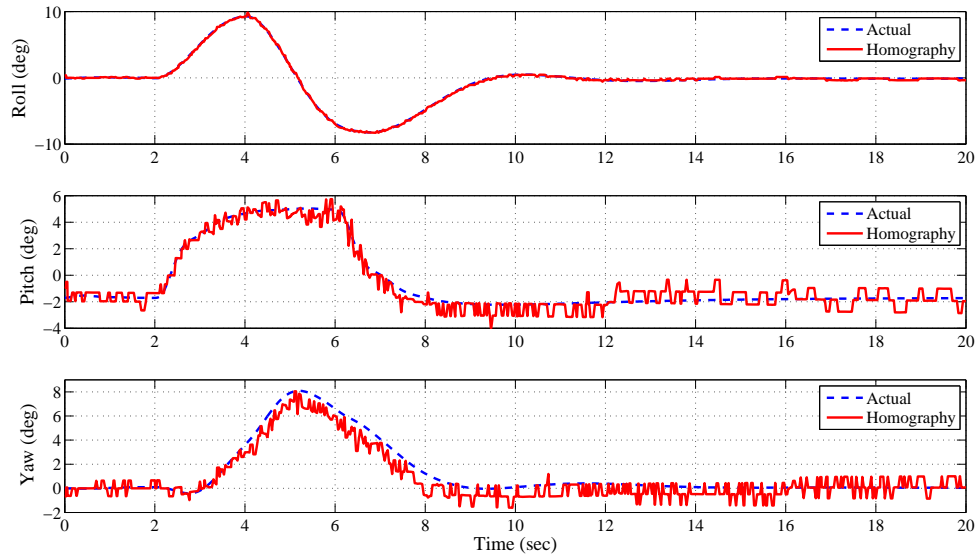


Figure 4–5: Actual attitude versus estimated attitude where the estimation is not part of the closed-loop control.

replacing the perfect position and attitude measurements, used in the guidance system and autopilot, with position and attitude estimations determined from the vision-based method. The resulting control architecture and sensor suite for this autonomous air vehicle is given in Figure 4–6. The noise content of the estimated position and attitude required filtering prior to being used by the autopilot, to prevent the high frequency noise from being passed to the aircraft actuators. As expected, the noise occurs at 30 Hz and corresponds to the frame rate of the camera. First-order, low pass-filters (cutoff frequency as low as 4 rad/sec) were used to filter the noise. The noise also prevented effective differentiation of the position and attitude and necessitated the use of rate gyros for yaw and roll damping, as depicted in Figure 4–6. The air data system is also included, as shown in Figure 4–6, for the initial altitude measurement, since it is more accurate for altitude than current GPS solutions. The results of the camera-in-the-loop system performing the same guidance commanded autonomous maneuver are given in Figures 4–7 and 4–8.

The simulation results indicate that a camera supplemented with minimal sensors such as rate gyros and barometric altitude can be used for completely autonomous flight of a fixed wing vehicle; however, some residual oscillation effects due to noise is present in the vehicle attitude response. A majority of the noise source can directly be attributed to camera pixilation effects and the corresponding phase lag introduced by the first order filtering.

4.2.5 Experimental Results

Based on the results of the simulation, a flight test experiment was conducted to establish the feasibility of the proposed vision-based state estimation method. Artificial features were placed along a stretch of the runway. A radio controlled aircraft with an onboard camera was flown over the runway. The video was overlaid with GPS data from a Garmin GPS 35 receiver. An example of a single frame of

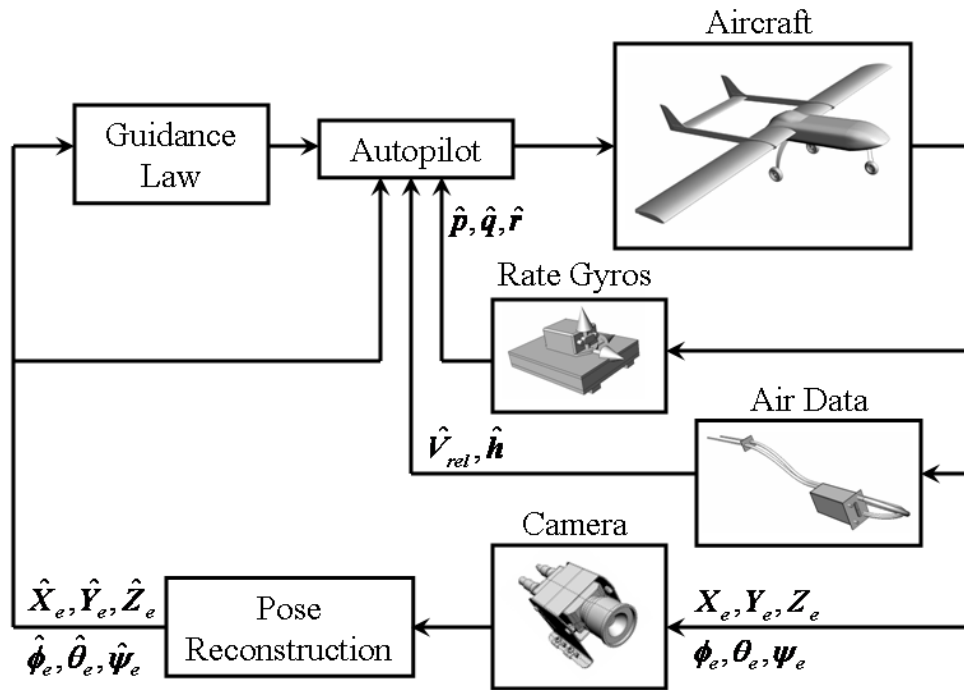


Figure 4-6: Autonomous control architecture.

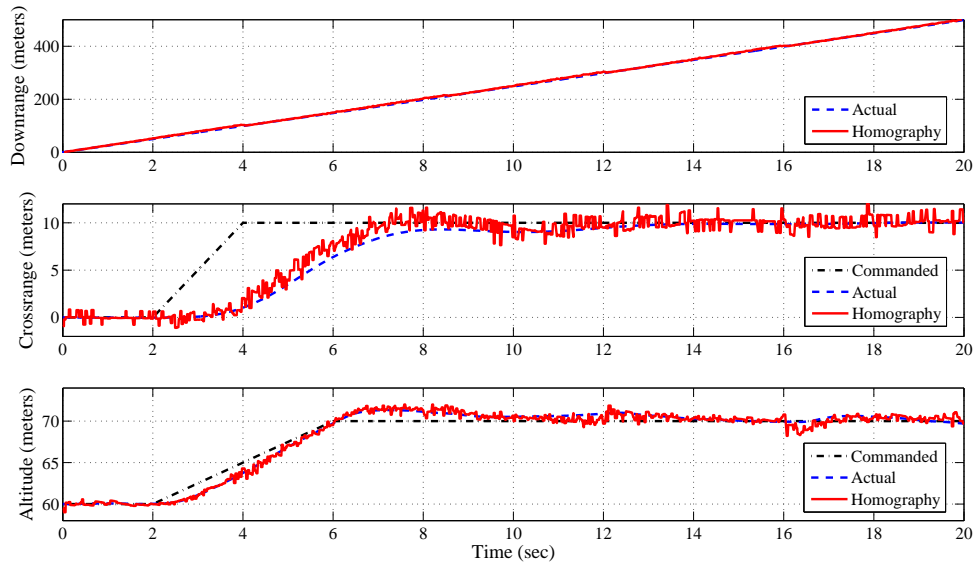


Figure 4-7: Actual translation versus estimated translation where the estimated value is used within the closed-loop control.

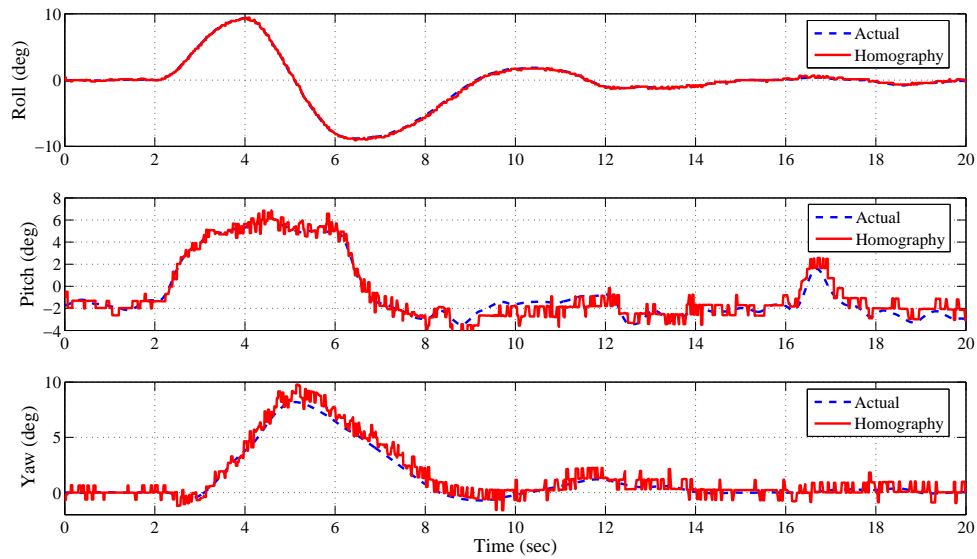


Figure 4–8: Actual attitude versus estimated attitude where the estimated value is used within the closed-loop control.

this video is given in Figure 4–10. A second GPS unit (manufactured by Eagle Tree Systems, LLC) was also onboard to test inter-GPS accuracy. The use of two GPS units provides comparison for the vision-based method, which is intended to compute GPS-like information. Video data was captured using a DV tape recorder and analyzed offline. A basic descriptive pictorial of what equipment was used (minus the eagle tree system) and the corresponding signal flow is given in Figure 4–9. See the Appendix for a more detailed description of the ground and airborne equipment. Due to poor image quality, including focus, motion blur and interlacing of the DV video, it became necessary to extract features by hand from individual frames. Features were extracted every sixth frame, resulting in a 5 Hz input signal.

Results of the experiment are given in Figure 4–11. In the legend for Figure 4–11, GPS2 represents the overlaid GPS data, and GPS1 represents the onboard data logger GPS values. A ‘*’ in the plot indicates a time when daisy-chaining was performed and pose reconstruction is performed using a new set of feature points.

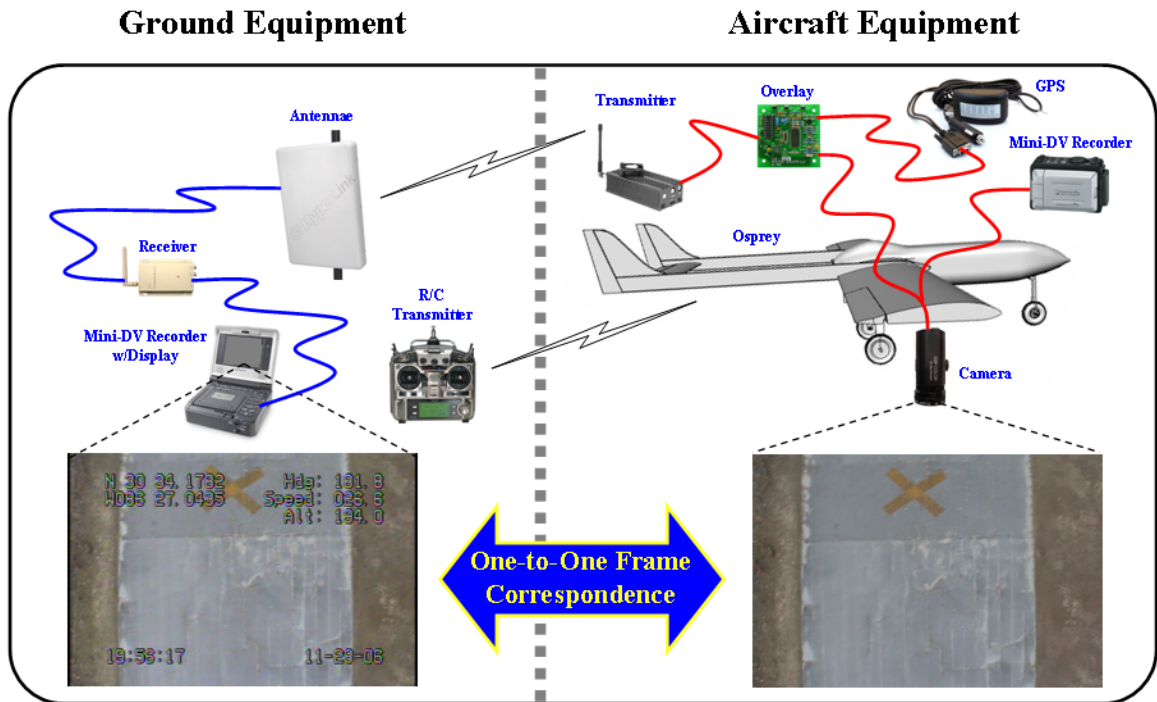


Figure 4-9: Overview of the flight test system and component interconnections.



Figure 4-10: Single video frame with GPS overlay illustrating landmarks placed along inside edge of the runway.

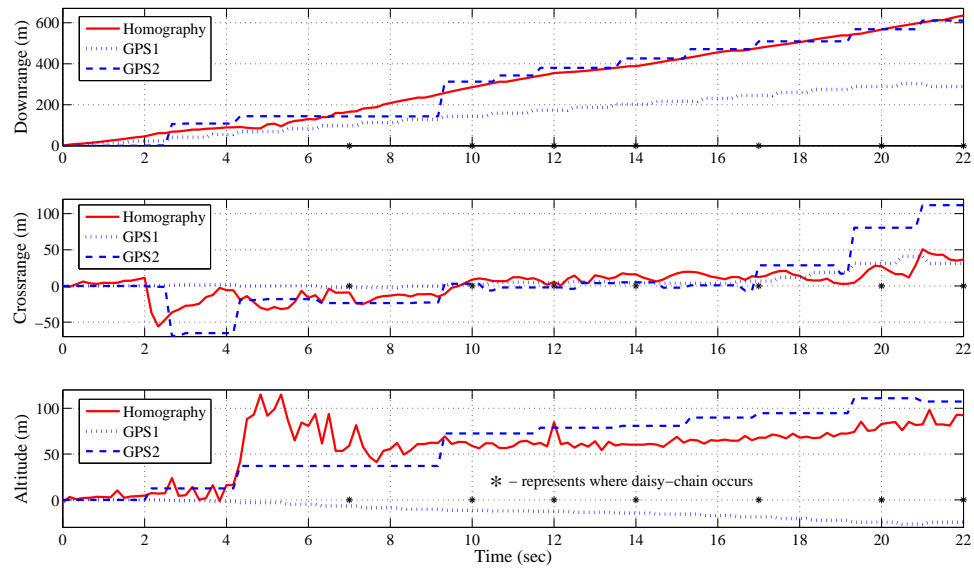


Figure 4–11: Experimental flight test results. Estimated position compared to two GPS signals.

The results from this test appear to be very promising. Significant mismatch exists between the two GPS measurements, and the vision-based estimation remains proportionate to the two GPS measurements. Furthermore, the estimates agree closely with GPS2 for downrange and crossrange translation, and with GPS1 for altitude translation. There is no discernible discontinuity or increased error at the daisy-chain handoff times. Note that the resolution of the vision-based estimation (5Hz) is also higher than that of both GPS units (1Hz). The pose estimation code can be executed in real time (>30Hz) on a typical laptop.

The accuracy of the GPS data, as recorded, is arguably dubious, therefore an alternate flight test was designed that was intended to enable the vehicle position to be determined with greater accuracy than what could be achieved with the inexpensive GPS units used in the first round of testing. In addition to the issues with the GPS output being used as "truth data", it was also of interest to investigate whether using a wider angle field of view lens on a more forward

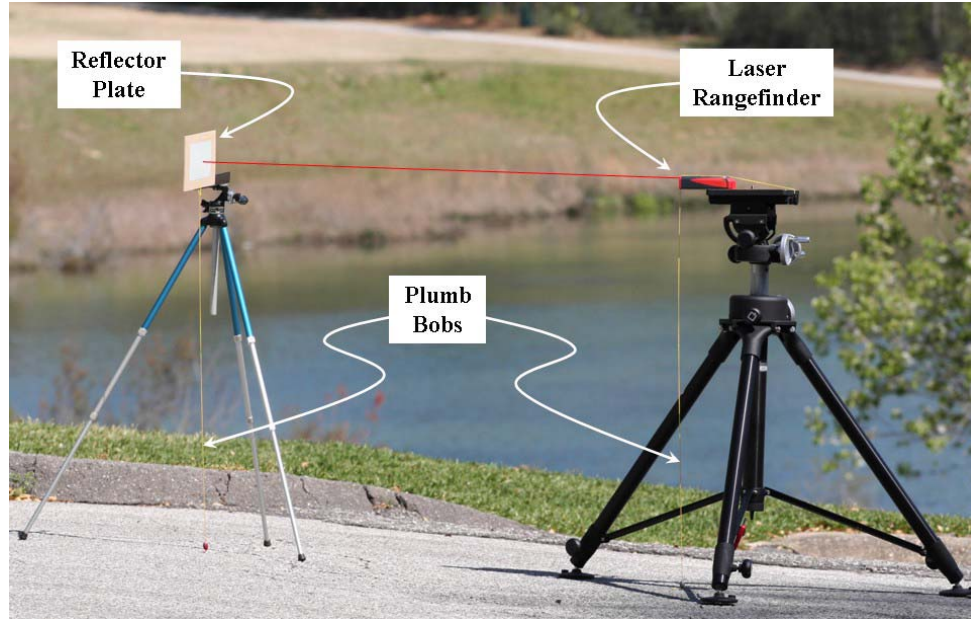


Figure 4–12: Technique for achieving accurate landmark relative placement distances.

pointing camera could improve the results. The fundamental assumption of this additional testing was that if the locations of the ground targets were known precisely, then the position of the vehicle could be ascertained more accurately through geometric reconstruction than what could be achieved with low cost GPS units.

Similar to before, plates/landmarks were placed along 274.32 meters (900 feet) of the runway. Unlike before, they were placed at 15.24 meter (50 foot) intervals where the accuracy of each plate location was known to within a few inches along the entirety of the 274.32 meters (900 feet) span. The two rows of plates, left and right of the runway centerline, were 18.59 meters (61 feet) apart. The plates were painted red so that a simplistic feature tracking algorithm could be used to locate and track their location in the image plane. The equipment that was used for surveying the landmarks is shown in Figure 4–12.

By using a wider field of view lens, the resulting video image exhibited severe lens distortion effects that required correcting in order for the homography to



Figure 4–13: Single video frame from second flight test experiment illustrating the effect of the more forward looking, wider field of view camera.

operate correctly. The distortion can be seen in Figure 4–13, where the four red landmarks in the lower portion of the frame appear to be located on a spherical surface as opposed to a plane; again, a fundamental requirement in the development of the homography method. This same image with the distortion removed is given in Figure 4–14. The interlacing effect, prevalent in Figure 4–10 has also been removed. As mentioned, the features were tracked and their trajectories in the image plane recorded using a simplistic ad-hoc scheme in Matlab. The pseudocode for tracking the four features of a single patch is given as:

Manually determine the location to initialize a 40x40 pixel window over each of the four landmarks in the first image

FOR all images containing the same patch of four landmarks

Read the next image in the sequence and assign it to an RGB color space array



Figure 4–14: Single video frame from second flight test experiment with the lens distortion removed.

Create a matrix equal to an element-by-element multiplication of the red space matrix with itself minus one tenth the element-by-element multiplication of the green space matrix with itself

FOR each of the four windows

Within the current window, threshold all values of the above defined matrix that are above 96% of the maximum value within the current window

The center of mass of this threshold value is chosen to be the pixel location representing the center of the landmark as it projects onto the image plane

Update the 40x40 pixel window to be centered over this pixel location

END FOR

Record the four pixel locations

END FOR

A 3-Dimensional plot of the matrix defined in the above pseudocode is given in Figure 4–15. Note that the large spikes correspond to the location of the red plates.

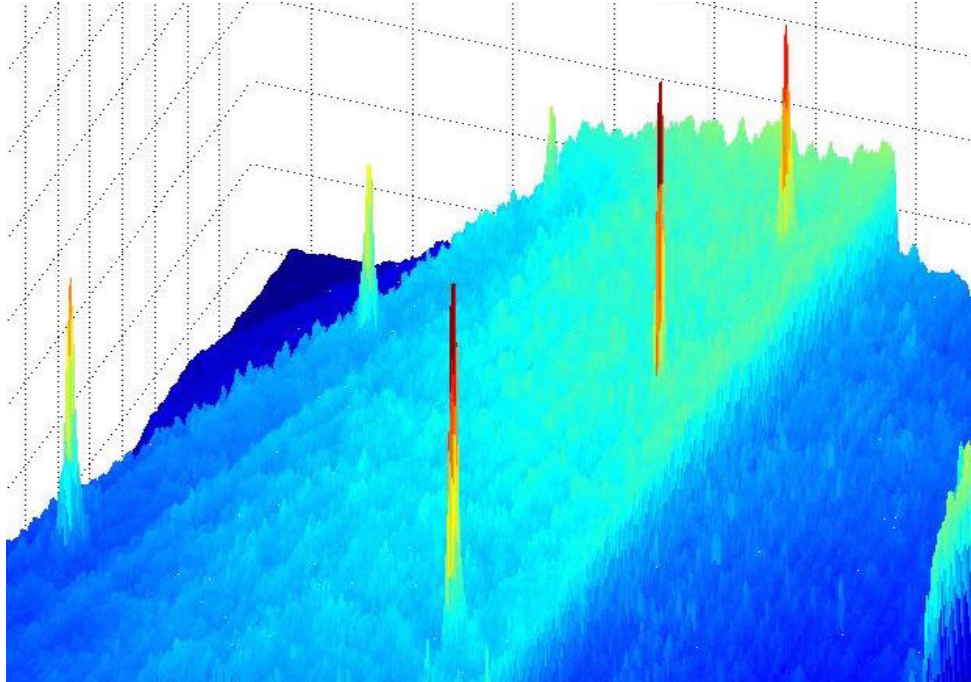


Figure 4–15: Example of a 3D color contour plot generated from the matrix designed as a nonlinear combination of the red and green color space matrices.

Values that are above 96% of the maximum value of each spike are thresholded and the centers-of-mass of these thresholded values are used to determine the predicted centers of the landmarks in the image frame. By following this procedure, it was predicted that sub-pixel accuracy could be achieved over simply selecting the pixel location of the maximum value or tip of the spike.

An example of the output of the above tracking algorithm is also given in Figure 4–16. The four trajectories in this particular case represent the trace of the landmarks from the first patch as it enters and exits the field of view (from top to bottom). As a point of interest, note that the center of the image plane does not correspond to location of the optical axis. This apparent oddity is in keeping with the camera calibration results and is most likely congruous with a low end imager and lens.

With the trajectories of the four landmarks of each patch recorded, vehicle localization can then be performed offline for analysis purposes. It should be pointed

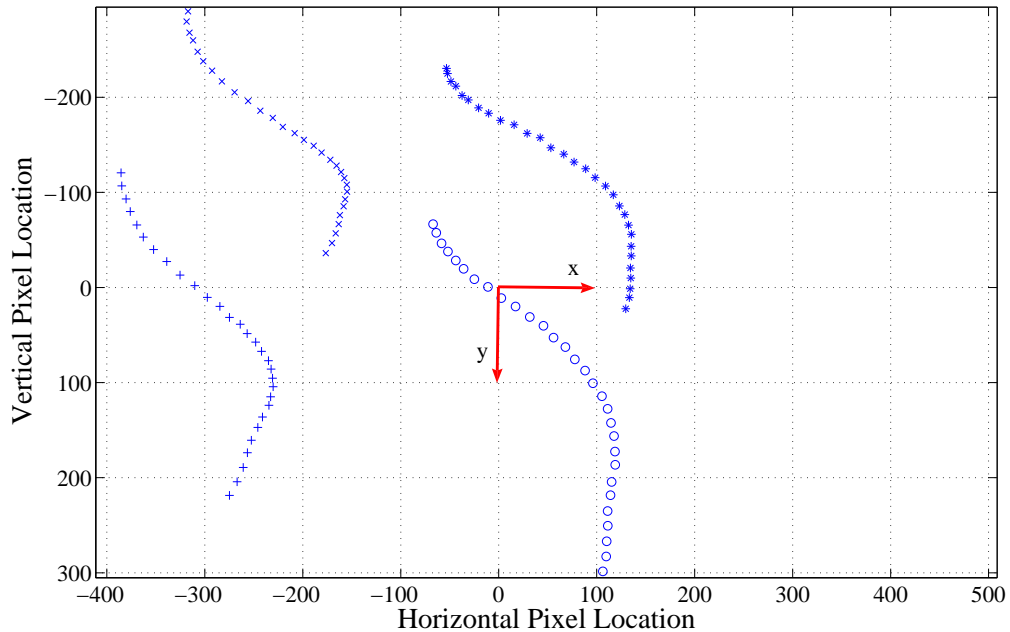


Figure 4–16: Image plane trajectories made by the landmarks from patch 1 entering and exiting the field of view.

out that the 40×40 pixel window is designed such that it is large enough to contain the landmark in the current frame and the subsequent frame. Smaller windows tended to not encapsulate both the current and subsequent frame landmarks due to vehicle motions between frames.

For a given set of three feature points, and knowledge of where those landmarks are in the earth frame, geometric reconstruction can be used to back out the location of the aircraft. This is illustrated in Figure 4–17, where in this particular illustration, a tetrahedron is used to determine the x_0 , y_0 , and z_0 location of the camera in the earth frame. e_1 , e_2 , and e_3 are known a priori relative distances between the 3 landmarks. Vertex angles η_1 , η_2 , and η_3 of the apex of the tetrahedron are determined by the focal length of the camera lens in pixel coordinates in conjunction with the pixel locations of where the landmarks corresponding to line segments e_1 , e_2 , and e_{12} occur in the image plane. The value for the skew, χ is used to account for the fact that the four landmarks most likely form a parallelogram,

since it was somewhat difficult to create a perfect rectangle in the field. In fact, e_{12} depends upon the skew, χ and is calculated according to

$$e_{12} = \sqrt{e_1^2 \sec^2(\chi) + e_2^2 + 2e_1 e_2 \sec(\chi) \sin(\chi)}$$

Presuming a , b , and c can be computed, then x_0 , y_0 , and z_0 of the camera can be determined via the following series of calculations:

$$\varphi_1 = \cos^{-1} \left(\frac{e_{12}^2 + c^2 - a^2}{2e_{12}c} \right)$$

$$\varphi_2 = \cos^{-1} \left(\frac{e_{12}^2 + e_2^2 - e_1^2}{2e_{12}e_2} \right)$$

and a' , shown in Figure 4–17, is calculated from the following

$$a' = \sqrt{e_2^2 \sec^2(\varphi_2) + c^2 - 2ce_2 \cos(\varphi_1) |\sec(\varphi_2)|}$$

If b is considered as a vector, the x and y direction cosines are given by, respectively

$$\cos \sigma_1 = \frac{e_2^2 + b^2 - c^2}{2e_2 b}$$

$$\cos \sigma_2 = \frac{e_2^2 \tan^2(\varphi_2) + b^2 - a'^2}{2e_2 \tan(\varphi_2) b}$$

Finally, the components of the position vector from the origin of the earth frame to the origin of the camera frame, in earth frame coordinates, is simply

$$x_0 = b \cos(\sigma_1)$$

$$y_0 = b \cos(\sigma_2)$$

$$z_0 = b \sqrt{\sin^2(\sigma_1) - \cos^2(\sigma_2)}$$

The difficulty of this method for pose estimation is in determining a , b , and c , more specifically, the edge lengths of the tetrahedron in Figure 4–17. The reason is that for given values of η_1 , η_2 , and η_3 and e_1 , e_2 , and e_{12} , there can be as little as zero physically possible solutions and as many as three distinctly different

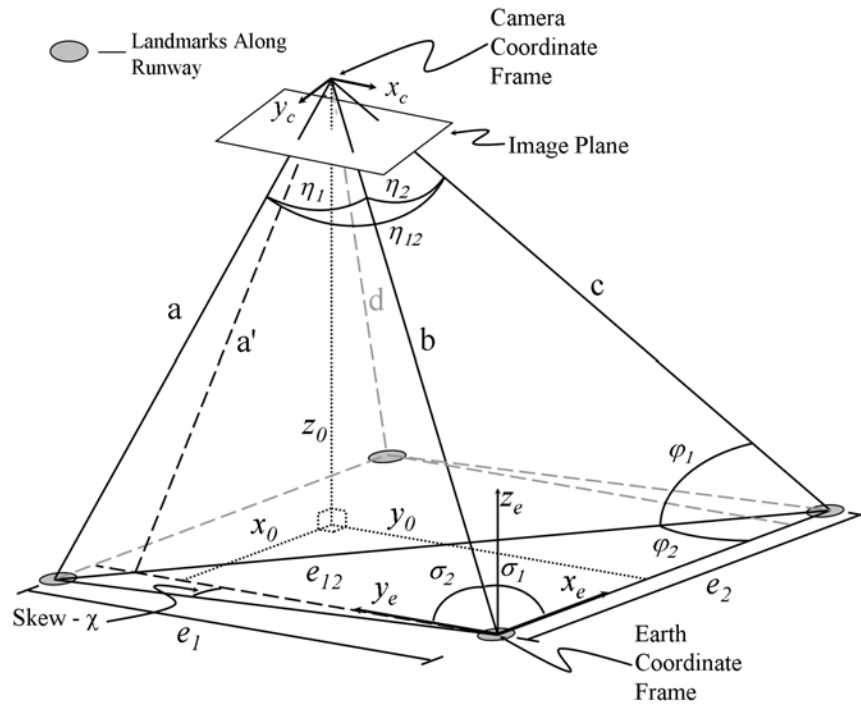


Figure 4–17: Basic concept of geometric position reconstruction from known landmark locations.

physically possible tetrahedrons. The possible values of a , b , and c are determined by simultaneously solving the three law-of-cosine rules for the three triangular facets making up the upright sides of the tetrahedron. A fourth landmark is needed to resolve the correct a , b , and c , via constructing multiple tetrahedrons, clocking around the four landmarks as shown in Figure 4–18, and selecting the a , b , c , and d that are common to all four tetrahedrons. Using this technique, each edge length is calculated three times. A merit of how reliable or accurate our position estimate is, and hence, how well the proper pixels representing the landmark centers were selected, is in how close each of the three edge length calculations a , b , c , and d are to each other. A quick convincing argument would be in the event that a , b , c , and d are the exact same in all 3 calculations, one could be very certain that they would consistently project and reproject back and forth between the camera and a surface containing 4 points with the same edge lengths e_1 , e_2 , e_3 , and e_4 .

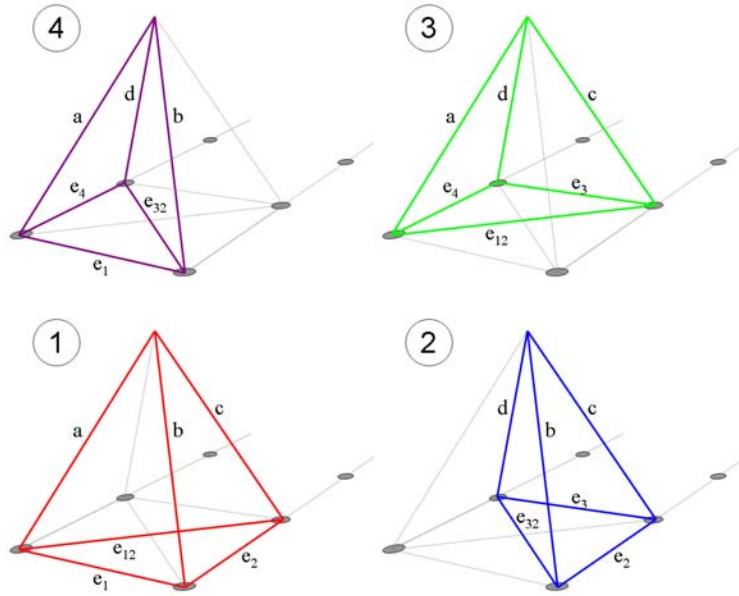


Figure 4–18: Illustration of how four tetrahedrons are used to estimate the length of each edge, a , b , c , & d three times.

If this surface can be shown to be a plane, then intuitively, this plane and four points would, with high confidence, be the earth plane and the points would be the centers of the landmarks. Results of this flight experiment are given in Figure 4–19. Because time was not recorded for this experiment, the ground track trajectory is given as opposed to downrange and crossrange time responses as given in Figure 4–11. The color variation in the geometric reconstruction represent the individual patches used along the length of the runway. The origin of the earth frame is placed at the first plate on the lower right that appears when the vision estimation begins. Also noteworthy, because this experiment used a somewhat forward looking camera, the camera position starts in the negative x -direction because the first plate is ahead of the camera; conversely, the camera is behind the first plate.

4.3 Conclusions

The efforts in this chapter integrated new vision-based pose estimation methods with the flight controls of an aerial vehicle in a guidance task. This method is based on Epipolar geometry, with a novel “daisy-chaining” approach

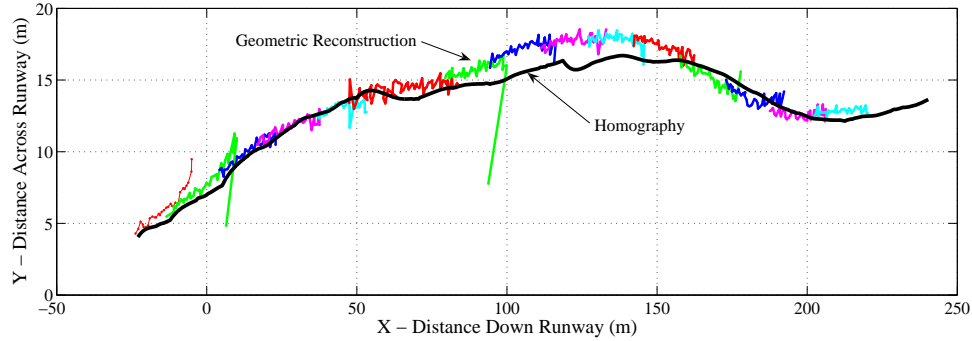


Figure 4-19: Second experimental flight test results. Estimated position compared to more accurate position from geometric reconstruction technique.

allowing image features to enter and leave the field of view while maintaining pose estimation. Furthermore, no known target is required.

The vision-based pose estimation method was verified experimentally with a radio controlled Osprey aircraft. Because the accuracy of the onboard GPS measurements was considered questionable, an alternate effort involving geometric reconstruction for position determination was undertaken to better represent truth data for validating the daisy-chaining pose estimation technique. To facilitate the experiments, a nonlinear aircraft flight model for the Osprey was developed to allow extensive simulation testing. Simulations include testing the pose estimation method in closed-loop control of the aircraft through an intentionally rigorous maneuver to evaluate the robustness of the technique.

The ultimate goal of this research is closed-loop control using camera data in place of GPS. To this end, future research will target online feature extraction, tracking, and pose estimation. Furthermore, a future task would be to investigate the use of nonlinear control techniques, such as discussed in the next chapter, to eliminate or reduce the amount of required a priori known information required in the estimation strategy. Additional sensor data such as IMU's and intermittent GPS could also be fused with the vision-based pose estimation to enhance performance.

CHAPTER 5
LYAPUNOV-BASED STATE ESTIMATION

5.1 Introduction

Many applications require the interpretation of the Euclidean coordinates of features of a 3-dimensional (3D) object through 2D images. In this chapter, the relative range and the Euclidean coordinates of a camera undergoing general affine motion are determined for pinhole camera systems via a nonlinear observer. The nonlinear observer asymptotically determines the range information provided that the motion parameters are known. The observer is developed through a Lyapunov-based design and stability analysis, and simulation results are provided that illustrate the performance of the state estimator. The contributions of this chapter are that the developed observer: can be applied to both affine and nonaffine systems; is continuous; and yields an asymptotic result.

5.2 Affine Euclidean Motion

For the development in this dissertation, the scenario of a moving camera viewing a static scene to recover the structure of the scene and/or the motion of the camera (cf., [53, 84, 85], and therein) is considered. The affine motion of the camera dynamics can be expressed as

$$\begin{bmatrix} \dot{x}_1 \\ \dot{x}_2 \\ \dot{x}_3 \end{bmatrix} = \begin{bmatrix} a_{11} & a_{12} & a_{13} \\ a_{21} & a_{22} & a_{23} \\ a_{31} & a_{32} & a_{33} \end{bmatrix} \begin{bmatrix} x_1 \\ x_2 \\ x_3 \end{bmatrix} + \begin{bmatrix} b_1 \\ b_2 \\ b_3 \end{bmatrix} \quad (5-1)$$

where $x(t) = [x_1(t), x_2(t), x_3(t)]^T \in \mathbb{R}^3$ denotes the unmeasurable Euclidean coordinates of the moving camera along the X , Y , and Z axes of a camera fixed reference frame, respectively, where the Z axis is colinear with the optical axis

of the camera. In (5–1), the parameters $a_{i,j}(t) \in \mathbb{R} \forall i, j = 1, 2, 3$ of the matrix $A(t) \in \mathbb{R}^{3 \times 3}$ and $b(t) = [b_1, b_2, b_3]^T \in \mathbb{R}^3$ denote the motion parameters. The affine motion dynamics introduced in (5–1) are expressed in a general form that describes an object motion consisting of a rotation, translation, and linear deformation [86].

Assumption 5.1: The motion parameters in $A(t)$ and $b(t)$ introduced in (5–1) are assumed to be known, bounded functions of time that are second order differentiable.(cf. [51, 55–60, 87–89]).

To illustrate how the affine dynamics in (5–1) represent a moving camera viewing a stationary object (see Figure 5–1), consider a feature point attached to a stationary object as in Figure 5–1. In Figure 5–1, \mathcal{F}_c denotes a body-fixed coordinate frame attached to the camera, \mathcal{I} denotes an inertial coordinate frame and $x(t)$ (expressed in \mathcal{F}_c) denotes the coordinates of the target feature point O_i . The linear and angular velocities of the target (i.e., $v_t(t)$ and $\omega_t(t)$) with respect to the camera (expressed in \mathcal{F}_c) can be written as

$$v_t = -Rv_c \quad \omega_t = -R\omega_c \quad (5-2)$$

where $R(t) \in \mathbb{R}^{3 \times 3}$ denotes the corresponding rotation between \mathcal{F}_c and \mathcal{I} , and $v_c(t)$ and $\omega_c(t)$ denote the linear and angular velocity of the camera, respectively. Based on (5–2), The time derivative of $x(t)$ can be expressed as

$$\dot{x} = [R\omega_c]^\times x + Rv_c = Ax + b. \quad (5-3)$$

Potential applications for this scenario under the restriction of Assumption 1 include examples where the camera is moving with a known/measurable linear and angular velocity where the goal is to estimate the Euclidean position of the moving camera in time, such as: inertial navigation in GPS denied environments and simultaneous localization and mapping (SLAM).

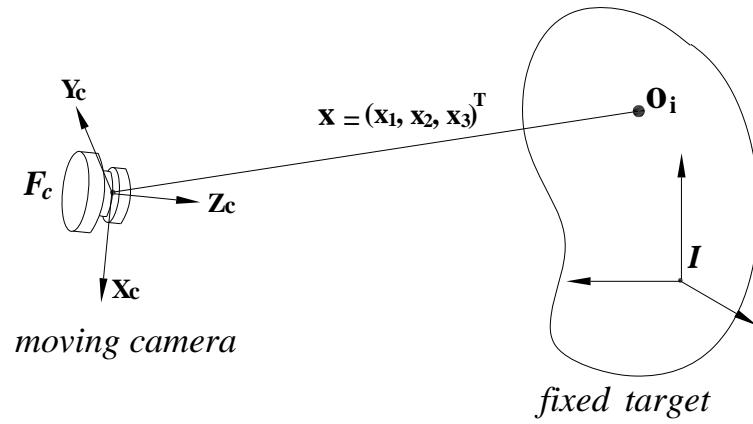


Figure 5-1: Moving camera stationary object scenario.

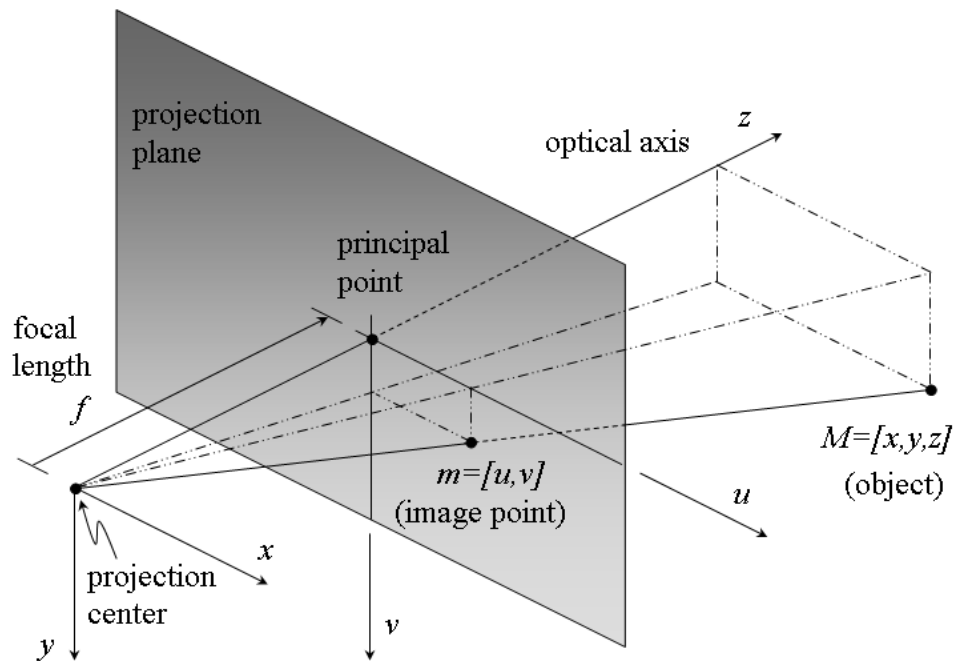


Figure 5-2: Euclidean point projected onto image plane of a pinhole camera

5.3 Object Projection

The projection of the coordinates $x(t)$ onto an image plane with its focus at the origin (see Figure 5-2) can be expressed as

$$p(t) \triangleq \begin{bmatrix} u & v \end{bmatrix}^T = \frac{f}{z} \begin{bmatrix} x & y \end{bmatrix}^T \quad (5-4)$$

where $f \in \mathbb{R}$ denotes the constant known distance between the focal point and the image plane.

Deriving the expression for the time rate of change of pixel location by taking the time derivative of (5-4) and utilizing (5-1) as

$$\dot{p}(t) = \Omega_1 + g, \quad (5-5)$$

where $\Omega_1(u, v, t) \in \mathbb{R}^2$ denotes a vector of measurable and known signals defined by

$$\Omega_1(t) \triangleq \begin{bmatrix} a_{11} & a_{12} & a_{13} \\ a_{21} & a_{22} & a_{23} \end{bmatrix} \begin{bmatrix} u \\ v \\ f \end{bmatrix} - \frac{1}{f} \begin{bmatrix} u \\ v \end{bmatrix} \begin{bmatrix} a_{31} & a_{32} & a_{33} \end{bmatrix} \begin{bmatrix} u \\ v \\ f \end{bmatrix} \quad (5-6)$$

and the unmeasurable signal $g(t) \triangleq [g_1(t), g_2(t)] \in \mathbb{R}^2$ is defined as

$$g(t) \triangleq \left\{ f \begin{bmatrix} b_1 \\ b_2 \end{bmatrix} - \begin{bmatrix} u \\ v \end{bmatrix} b_3 \right\} \frac{1}{z}. \quad (5-7)$$

From the above definition for $g(t)$, the following expression can be written:

$$\begin{aligned} g_1^2 + g_2^2 &= \left\{ (fb_1 - ub_3) \frac{1}{z} \right\}^2 + \left\{ (fb_2 - vb_3) \frac{1}{z} \right\}^2 \\ &= [(fb_1 - ub_3)^2 + (fb_2 - vb_3)^2] \left\{ \frac{1}{z} \right\}^2. \end{aligned} \quad (5-8)$$

Based upon (5-8) the time varying depth estimation can be expressed as,

$$z = \sqrt{\frac{(fb_1 - ub_3)^2 + (fb_2 - vb_3)^2}{g_1^2 + g_2^2}} \quad (5-9)$$

Assumption 5.2: The image-space feature coordinates $u(t)$, $v(t)$ are bounded functions of time.

Assumption 5.3: If $g(t)$ can be identified, then $z(t)$ can be determined from (5-7), provided $b_1, b_2, b_3 \neq 0$ simultaneously. This observability assumption physically means that the object must translate in at least one direction.

Remark 5.1: Based on Assumptions 5.1-5.3, the expressions given in (5-5)-(5-9) can be used to determine that $\dot{p}(t)$, $\Omega_1(t)$, and $g(t) \in \mathcal{L}_\infty$. Given that these signals are bounded, Assumptions 5.1-5.3 can be used to prove that

$$\|g(\cdot)\| \leq \zeta_1 \quad \|\dot{g}(\cdot)\| \leq \zeta_2 \quad \|\ddot{g}(\cdot)\| \leq \zeta_3 \quad (5-10)$$

where ζ_1, ζ_2 and $\zeta_3 \in \mathbb{R}$ denote known positive constants.

5.4 Range Identification For Affine Systems

5.4.1 Objective

The objective of this section is to extract the Euclidean coordinate information of the object feature from its image-based projection. From (5-4) and the fact that $u(t)$, and $v(t)$ are measurable, if $z(t)$ could be identified, then the complete Euclidean coordinates of the feature can be determined. To achieve this objective, an estimator is constructed based on the unmeasurable image-space dynamics for $p(t)$. To quantify the objective, a measurable estimation error, denoted by $e(t) \triangleq [e_1(t), e_2(t)]^T \in \mathbb{R}^2$, is defined as follows:

$$e = p - \hat{p} \quad (5-11)$$

where $\hat{p}(t) \triangleq [\hat{p}_1(t), \hat{p}_2(t)]^T \in \mathbb{R}^2$ denotes a subsequently designed estimate. An unmeasurable¹ filtered estimation error, denoted by $r(t) \triangleq [e_1(t), e_2(t)]^T \in \mathbb{R}^2$, is also defined as

$$r = \dot{e} + \alpha e \quad (5-12)$$

where $\alpha \in \mathbb{R}^{2 \times 2}$ denotes a diagonal matrix of positive constant gains $\alpha_1, \alpha_2 \in \mathbb{R}$. Motivation for the development of the filtered estimation error in (5-12), is that the subsequent observer is based on the equation (5-5). If $g(t)$ in (5-5) can be identified, the fact that the feature point coordinates $p_i(t) \forall i = 1, 2$ are measurable can be used along with (5-9) to compute $z(t)$ provided the observability condition in Assumption 5.3 is satisfied.

5.4.2 Estimator Design and Error System

Based on (5-5) and the subsequent analysis, the following estimation signals are defined:

$$\dot{\hat{p}}(t) = \Omega_1 + \hat{g} \quad (5-13)$$

where $\hat{g}(t) \triangleq [\hat{g}_1(t), \hat{g}_2(t)]^T \in \mathbb{R}^2$ denotes a subsequently designed estimate for $g(t)$. The following error dynamics are obtained after taking the time derivative of $e(t)$ and utilizing (5-5) and (5-13):

$$\dot{e} = g - \hat{g}. \quad (5-14)$$

Based on the structure of (5-12) and (5-14), $\dot{\hat{g}}(t)$ is designed as follows [56]:

$$\dot{\hat{g}} = -(k_s + \alpha)\hat{g} + \gamma \text{sgn}(e) + \alpha k_s e \quad (5-15)$$

where $k_s, \gamma \in \mathbb{R}^{3 \times 3}$ denote diagonal matrices of positive constant estimation gains, and the notation $\text{sgn}(\cdot)$ is used to indicate a vector with the standard signum

¹ The filtered estimation signal is unmeasurable due to a dependence on the unmeasurable terms $g_1(t), g_2(t)$.

function applied to each element of the argument. The structure of the estimator in (5–15) contains discontinuous terms; however, as discussed in [56], the overall structure of the estimator is continuous (i.e., $\hat{g}(t)$ is continuous). After using (5–12), (5–14), and (5–15), the following expression can be obtained:

$$\dot{r} = \eta - k_s r - \gamma \text{sgn}(e) \quad (5-16)$$

where $\eta(t) \triangleq \begin{bmatrix} \eta_1 & \eta_2 \end{bmatrix}^T \in \mathbb{R}^2$ is defined as

$$\eta = \dot{g} + (k_s + \alpha) g. \quad (5-17)$$

Based on (5–10) and (5–17), the following inequalities can be developed:

$$|\eta(\cdot)| \leq \zeta_4 \quad |\dot{\eta}(\cdot)| \leq \zeta_5. \quad (5-18)$$

where ζ_4 and $\zeta_5 \in \mathbb{R}$ denote known positive constants.

Remark 5.1: Considering (5–9), the unmeasurable signal $z(t)$ can be identified if $\hat{g}(t)$ approaches $g(t)$ as $t \rightarrow \infty$ (i.e., $\hat{u}(t)$ and $\hat{v}(t)$ approach $u(t)$ and $v(t)$ as $t \rightarrow \infty$) since the parameters $b_i(t) \forall i = 1, 2$ are assumed to be known, and $u(t)$ and $v(t)$ are measurable. After $z(t)$ is identified, (5–4) can be used to extract the 3D Euclidean coordinates of the object feature (i.e. determine the range information). To prove that $\hat{g}(t)$ approaches $g(t)$ as $t \rightarrow \infty$, the subsequent development will focus on proving that $\|\dot{e}(t)\| \rightarrow 0$ and $\|e(t)\| \rightarrow 0$ as $t \rightarrow \infty$ based on (5–11) and (5–14).

5.5 Analysis

The following theorem and associated proof can be used to conclude that the observer design of (5–13) and (5–15) can be used to identify the unmeasurable signal $z(t)$.

Theorem 5.1: For the system in (5–5)-(5–7), the unmeasurable signal $z(t)$ (and hence, the Euclidean coordinates of the object feature) can be asymptotically

determined from the estimator in (5–13) and (5–15) provided the elements of the constant diagonal matrix γ introduced in (5–15) are selected according to the sufficient condition

$$\gamma_i \geq \zeta_4 + \frac{1}{\alpha_i} \zeta_5 \quad (5-19)$$

$\forall i = 1, 2$, where ζ_4, ζ_5 are defined in (5–18).

Proof: Consider a non-negative function $V(t) \in \mathbb{R}$ as follows (i.e., a Lyapunov function candidate):

$$V = \frac{1}{2} r^T r . \quad (5-20)$$

After taking the time derivative of (5–20) and substituting for the error system dynamics given in (5–16), the following expression can be obtained:

$$\dot{V} = -r^T k_s r + (\dot{e} + \alpha e)^T (\eta - \gamma \text{sgn}(e)) . \quad (5-21)$$

After integrating (5–21) and exploiting the fact that

$$\xi_i \cdot \text{sgn}(\xi_i) = |\xi_i| \quad \forall \xi_i \in \mathbb{R},$$

the following inequality can be obtained:

$$V(t) \leq V(t_0) - \int_{t_0}^t (r^T(\sigma) k_s r(\sigma)) d\sigma + \sum_{i=1}^2 \alpha_i \int_{t_0}^t |e_i(\sigma)| (|\eta_i(\sigma)| - \gamma_i) d\sigma + \chi_i, \quad (5-22)$$

where the auxiliary terms $\chi_i(t) \in \mathbb{R}$ are defined as

$$\chi_i = \int_{t_0}^t \dot{e}_i(\sigma) \eta_i(\sigma) d\sigma - \gamma_i \int_{t_0}^t \dot{e}_i(\sigma) \text{sgn}(e_i(\sigma)) d\sigma \quad (5-23)$$

$\forall i = 1, 2$. The integral expression in (5–23) can be evaluated as

$$\begin{aligned} \chi_i &= e_i(\sigma) \eta_i(\sigma) \Big|_{t_0}^t - \int_{t_0}^t e_i(\sigma) \dot{\eta}_i(\sigma) d\sigma - \gamma_i |e_i(\sigma)| \Big|_{t_0}^t \\ &= e_i(t) \eta_i(t) - \int_{t_0}^t e_i(\sigma) \dot{\eta}_i(\sigma) d\sigma - \gamma_i |e_i(t)| - e_i(t_0) \eta_i(t_0) + \gamma_i |e_i(t_0)| \end{aligned} \quad (5-24)$$

$\forall i = 1, 2$. Substituting (5-24) into (5-22) and performing some algebraic manipulation yields

$$V(t) \leq V(t_0) - \int_{t_0}^t (r^T(\sigma) k_s r(\sigma)) d\sigma + \chi_3 + \zeta_0$$

where the auxiliary terms $\chi_3(t)$, $\zeta_0 \in \mathbb{R}$ are defined as

$$\chi_3 = \sum_{i=1}^2 \alpha_i \int_{t_0}^t |e_i(\sigma)| \left(|\eta_i(\sigma)| + \frac{1}{\alpha_i} |\dot{\eta}_i(\sigma)| - \gamma_i \right) d\sigma + \sum_{i=1}^2 |e_i(t)| (|\eta_i(t)| - \gamma_i)$$

$$\zeta_0 = \sum_{i=1}^2 -e_i(t_0) \eta_i(t_0) + \gamma_i |e_i(t_0)|.$$

Provided $\gamma_i \forall i = 1, 2$ are selected according to the inequality introduced in (5-19), $\chi_3(t)$ will always be negative or zero; hence, $V(t)$ can be upper bounded as

$$V(t) \leq V(t_0) - \int_{t_0}^t (r^T(\sigma) k_s r(\sigma)) d\sigma + \zeta_0. \quad (5-25)$$

From (5-20) and (5-25), the following inequalities can be determined:

$$V(t_0) + \zeta_0 \geq V(t) \geq 0;$$

hence, $r(t) \in \mathcal{L}_\infty$. The expression in (5-25) can be used to determine that

$$\int_{t_0}^t (r^T(\sigma) k_s r(\sigma)) d\sigma \leq V(t_0) + \zeta_0 < \infty. \quad (5-26)$$

By definition, (5-26) can now be used to prove that $r(t) \in \mathcal{L}_2$. From the fact that $r(t) \in \mathcal{L}_\infty$, (5-11) and (5-12) can be used to prove that $e(t)$, $\dot{e}(t)$, $\hat{p}(t)$, and $\dot{\hat{p}}(t) \in \mathcal{L}_\infty$. The expressions in (5-13) and (5-15) can be used to determine that $\hat{g}(t)$ and $\dot{\hat{g}}(t) \in \mathcal{L}_\infty$. Based on (5-10), the expressions in (5-16) and (5-17) can be used to prove that $\eta(t)$, $\dot{\eta}(t)$, $\dot{r}(t) \in \mathcal{L}_\infty$. Based on the fact that $r(t)$, $\dot{r}(t) \in \mathcal{L}_\infty$ and that $r(t) \in \mathcal{L}_2$, Barbalat's Lemma [90] can be used to prove that $\|r(t)\| \rightarrow 0$ as $t \rightarrow \infty$; hence, standard linear analysis can be used to prove that $\|e(t)\| \rightarrow 0$ and $\|\dot{e}(t)\| \rightarrow 0$ as $t \rightarrow \infty$. Based on the fact that $\|e(t)\| \rightarrow 0$ and $\|\dot{e}(t)\| \rightarrow 0$ as $t \rightarrow \infty$, the expression given in (5-11) can be used to determine that $\hat{p}_1(t)$ and

$\hat{p}_3(t)$ approach $p_1(t)$ and $p_3(t)$ as $t \rightarrow \infty$, respectively. Therefore, the expression in (5–14) can be used to determine that $\hat{g}(t)$ approaches $g(x)$ as $t \rightarrow \infty$. The result that $\hat{g}(t)$ approaches $g(t)$ as $t \rightarrow \infty$, the fact that the parameters $b_i(t) \forall i = 1, 2, 3$ are assumed to be known, and the fact that the image-space signals $p_1(t)$ and $p_3(t)$ are measurable can be used to identify the unknown signal $z(t)$ from (5–9). Once $z(t)$ is identified, the complete Euclidean coordinates of the object feature can be determined using (5–4).

With the Euclidean coordinates of the object known, a simplistic method for determining aircraft altitude above the ground could employ the following relationship:

$$h = x \sin \phi \cos \theta + y \{ \cos \phi \cos \theta \cos \rho + \sin \theta \sin \rho \} + z \{ \cos \phi \cos \theta \sin \rho - \sin \theta \cos \rho \}$$

where ρ is the downward look angle of the camera with respect to the aircraft and ϕ and θ represent the aircraft roll and pitch angle respectively.

5.6 Conclusion

The results in this chapter focus on the use of a nonlinear estimator to determine the range and the Euclidean coordinates of an object feature with respect the camera coordinate system undergoing general affine motion. The nonlinear estimator is proven, via a Lyapunov-based analysis, to asymptotically determine the range information for a camera system with known motion parameters. If specific observability conditions are satisfied, the identified range can be used to reconstruct the Euclidean coordinates of the moving aircraft with respect to a fixed object on the ground .

CHAPTER 6 CONTRIBUTIONS AND FUTURE WORK

A novel vision-based estimation, localization, and control methodology is presented for enabling autonomous flight of a fixed-wing air vehicle; providing it with the capability of flying indefinitely over a region composed of planar patches of feature points. The proposed daisy-chaining approach is distinct from the majority of the current vision-based methods of state estimation in that current methods usually require some degree of a priori knowledge of landmarks or are specifically designed for hovering vehicles and therefore are not devised to handle feature points entering and leaving the field-of-view of the camera. One contribution of this dissertation is that it is the first occasion that a homography-based state estimation method is presented to handle feature points entering and leaving the camera field-of-view. As a result, this is also the first time in which a camera has been demonstrated to act as the sole sensor, with the exception of an altimeter for approximating height above a given planar patch, for estimating aircraft position during flight into a GPS denied environment. As a compliment to these results and to address the requirement for an estimation of the height above a given planar patch, a Lyapunov-based state estimator, used in combination with the daisy-chaining method, is the first instance of illustrating the plausibility of autonomous air vehicle flight over an indefinite distance with the camera “truly” acting as the sole vehicle sensor.

Using a video camera as the primary sensor in aircraft control requires special consideration from a controls standpoint. In addition to such presented concerns, as the air vehicle is required to fly in lesser benign regimes, such as with agile maneuvering, it becomes evident that simplistic classical control methods will be

limited in capability and performance. Therefore, in order to fly an aircraft in a closed-loop sense using a camera as a primary sensor, the controller needs to be robust to not only parametric uncertainties, but to system noise that is of the kind uniquely characteristic of camera systems. A novel nonlinear controller is presented as a credible answer to such anticipated issues, resulting in the first case of developing an aircraft controller for an uncertain system that provides a semi-global asymptotically stable result, where there exists input uncertainty as well as generalized additive nonlinear disturbances that are state and time varying. Future work on this control approach should attempt to eliminate the requirement that the filtered tracking error needs to be measured, as opposed to the more desirable situation of simply measuring the tracking error.

Other possible future work that builds upon what is presented in this dissertation would be to investigate methods that would allow the relaxation of the coplanar requirement, i.e. navigation over a non-flat earth, to fuse the homography-based daisy-chain estimates with additional sensors for improved accuracy, and to perform a comparison analysis by applying estimation methods (i.e. Kalman filtering) to both feature point tracking in the image plane as well as vehicle state estimation. Potential future work might also be to investigate multiple vehicles for use in the homography-based daisy-chaining method as an analogue to what is currently being researched within the field of cooperative-SLAM.

Because error from the homography-based daisy-chain estimate accumulates with each handoff, it would also be of interest to perform flight experiments that combine the Lyapunov-based state estimator with the daisy-chaining method. In doing so, one could investigate using an updated height above planar patch measurement between each hand-off to reduce the effect of accumulating position error. This improvement would be expected since position error scales with the error in the estimated magnitude of the vector that is defined by being both normal

to the planar patch and extending from the planar patch to the vehicle. The current method uses height above ground derived from an altimeter to approximate this magnitude, which ultimately results in an error in estimated position. Finally, the ultimate goal of such a blending of methodologies would be in demonstrating autonomous flight via the camera as the sole sensor.

Future efforts should also attempt to mitigate the estimation errors that can directly be attributed to the fidelity of the equipment used. To address this issue and to support future work, recent purchases of the following higher quality equipment have been made:

- SolidLogic C156 Mini-ITX System, EPIA MII 12000G Mainboard, for direct-to-hard-disk video recording and possible real-time onboard processing.
- Pixelink PL-B958F 2.0 megapixel (1600 x 1200) color CCD camera based upon the Sony ICX274 progressive scan sensor with a $\frac{1}{2}$ " optical format, global shutter, variable shutter speed and frame rate, and standard FireWire (1394A).
- Hauppauge WinTV-PVR-USB2, direct-to-hard-disk video recorder for recording the air-vehicle-to-ground telemetered video signal.

APPENDIX A
(CHAPTER 3) INTEGRATION OF THE AUXILIARY FUNCTION, $L(t)$

(See Lemma 1) Integrating both sides of (3–37) yields

$$\int_0^t L(\tau) d\tau = \int_0^t r(\tau)^T \left(N_d(\tau) - \beta \tilde{\Omega} \text{sgn}(e(\tau)) \right) d\tau. \quad (\text{A-1})$$

Substituting (3–16) into (A–1), utilizing (3–29), and rearranging yields

$$\begin{aligned} \int_0^t L(\tau) d\tau &= \int_0^t \left(\frac{\partial e(\tau)}{\partial \tau} \right)^T N_d(\tau) d\tau - \int_0^t \left(\frac{\partial e(\tau)}{\partial \tau} \right)^T \beta \Lambda \text{sgn}(e(\tau)) d\tau \\ &+ \int_0^t \alpha e(\tau)^T (N_d(\tau) - \beta \Lambda \text{sgn}(e(\tau))) d\tau - \int_0^t r(\tau)^T \beta \Delta \text{sgn}(e(\tau)) d\tau. \end{aligned} \quad (\text{A-2})$$

Integrating the first integral in (A–2) using integration by parts,

$$\begin{aligned} \int_0^t L(\tau) d\tau &= e(\tau)^T N_d(\tau) \Big|_0^t - \int_0^t e(\tau)^T \frac{\partial N_d(\tau)}{\partial \tau} d\tau - \int_0^t \left(\frac{\partial e(\tau)}{\partial \tau} \right)^T \beta \Lambda \text{sgn}(e(\tau)) d\tau \\ &+ \int_0^t \alpha e(\tau)^T (N_d(\tau) - \beta \Lambda \text{sgn}(e(\tau))) d\tau - \int_0^t r(\tau)^T \beta \Delta \text{sgn}(e(\tau)) d\tau. \end{aligned} \quad (\text{A-3})$$

From (A–3), the following bound can be obtained:

$$\begin{aligned} \int_0^t L(\tau) d\tau &\leq \int_0^t \alpha \|e(\tau)\| \left(\|N_d(\tau)\| + \frac{1}{\alpha} \left\| \frac{\partial N_d(\tau)}{\partial \tau} \right\| - \beta \lambda_{\min}(\Lambda) \right) d\tau \\ &+ \|e(t)\| (\|N_d(t)\| - \beta \lambda_{\min}(\Lambda)) + \beta \|\Lambda\| \|e(0)\| - e(0)^T N_d(0) \\ &+ \sqrt{m} \int_0^t \beta \|\Delta\| \|r(\tau)\| d\tau, \end{aligned} \quad (\text{A-4})$$

where m was defined in (3–1). Thus, it is clear from (A–4) that if β satisfies (3–33), then (3–38) holds.

APPENDIX B
(CHAPTER 4) VIDEO EQUIPMENT USED ONBOARD THE AIRCRAFT

The items listed in this appendix represent the equipment that was flown on the aircraft as part of the flight experiment:

Figure B-1 is of the 640 x 480 pixel CCD bullet camera that was used for the video collection. The output signal from this camera was split with a Y-cable and sent to two different devices.

Figure B-2 shows the mini DV recorder that was used. It was determined through several unsuccessful attempts to gather video data that it was necessary to have the ability to record onboard in order capture video data that was noise free. The video from the camera in Figure B-1 was split with a Y-cable, as previously stated, with one of the video signals going directly into this recorder.

Figure B-3 is of the self contained GPS antennae/receiver. This was used to determine the location of the aircraft, which in turn was used initially as truth data. The daisy-chain results were compared with the GPS data for validation



Figure B-1: Sony Color Exview SuperHAD (480 Lines of Resolution)



Figure B-2: Panasonic AG-DV1 Digital Video Recorder



Figure B-3: Garmin GPS 35 OEM GPS Receiver

purposes. The output from this device went to the GPS overlay board shown in Figure B-4.

Figure B-4 is of the GPS overlay board. The other video signal from the Y-cable coming from the camera in Figure B-1 went into this board that overlaid the video with the GPS data from the receiver shown in Figure B-3. From here, the overlaid video was sent to the transmitter shown in Figure B-5.

Figure B-5 is of the transmitter that was used to send the GPS overlaid video signal to the ground receiver.



Figure B-4: Intuitive Circuits, LLC - OSD-GPS Overlay Board

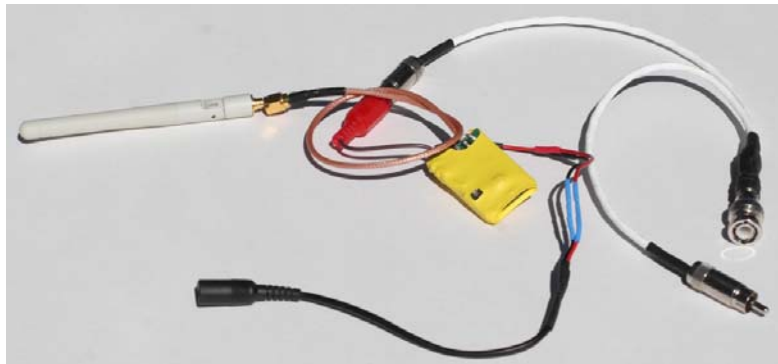


Figure B-5: 12V, 2.4Ghz, 100mW, Video Transmitter and Antennae



Figure B-6: Eagle Tree, Seagull, Wireless Dashboard Flight System - Pro Version: (1) Wireless Telemetry Transmitter, (2) Eagle Tree Systems G-Force Expander, and (3) Eagle Tree Systems GPS Expander

Figure B-6 is of the secondary GPS receiver that was also used for comparison purposes. This device telemetered the data down on a separate frequency, where it was recorded on a ground station.

APPENDIX C
(CHAPTER 4) GROUND SUPPORT EQUIPMENT

The items listed in this appendix correspond to the ground equipment used in the flight experiment:

Figure C-1 is of the video receiver that received the GPS overlaid video.

Figure C-2 is of the second video recorder that was used in the testing. In this case, it was used to record the transmitted GPS overlaid video. The reason for requiring a second video was that it was necessary to have a clean video for performing the analysis with (see Figure B-2), yet a method was needed to correlate each frame of the clean video with a GPS location. Having two recorders operating at once was the simplest solution. The video that was captured on this device could not be used for analysis due to the RF noise and the overlay text that took up much of the image. By doing a frame by frame comparison with the clean video recorded by the recorder in Figure B-2, it was possible to ascertain the position of the vehicle to within 1 second (GPS frequency) of every frame of the clean video.

Figure C-3 is the groundstation interface for the secondary GPS receiver that was used, shown in Figure B-6.



Figure C-1: RX-2410 2.4 GHz Wireless 4-channel Audio/Video Selectable Receiver



Figure C-2: Sony GV-D1000 Portable MiniDV Video Walkman



Figure C-3: Eagle Tree, Seagull, Real-time Data Dashboard, Wireless Telemetry Data, Receiver Model STR-01



Figure C-4: Leica DISTO™ A5 (Measuring Range up to 650 ft, Accuracy +/- 0.06 inches)

Figure C-4 is the laser rangefinder, shown in Figure 4-12, that was used in the accurate placement of the landmarks.

REFERENCES

- [1] A. Moutinho and J. R. Azinheira, “Stability and Robustness Analysis of the AURORA Airship Control System Using Dynamic Inversion,” *Proceedings of the International Conference on Robotics and Automation*, Barcelona, Spain, April 2005, pp. 2265–2270.
- [2] M. W. Oppenheimer and D. B. Doman, “Control of an Unstable, Nonminimum Phase Hypersonic Vehicle Model,” *Proceedings of the IEEE Aerospace Conference*, Big Sky, MT, March 2006, pp. 1-7.
- [3] S. Onori, P. Dorato, S. Galeani, and C. Abdallah, “Finite Time Stability Design Via Feedback Linearization,” *Proceedings of the Conference on Decision and Control, and the European Control Conference*, Seville, Spain, December 2005, pp. 4915-4920.
- [4] Z. Szabo, P. Gaspar, and J. Bokor, “Tracking Design for Wiener Systems Based on Dynamic Inversion,” *Proceedings of the International Conference on Control Applications*, Munich, Germany, October 2006, pp. 1386–1391.
- [5] J. Chen, D. Li, X. Jiang, and X. Sun, “Adaptive Feedback Linearization Control of a Flexible Spacecraft,” *Proceedings of the Conference on Intelligent Systems Design and Applications*, Jinan, China, October 2006, pp. 225–230.
- [6] A. D. Ngo and D. B. Doman, “Dynamic Inversion-Based Adaptive/Reconfigurable Control of the X-33 on Ascent,” *Proceedings of the IEEE Aerospace Conference*, Big Sky, MT, March 2006, pp. 2683–2697.
- [7] M. D. Tandale and J. Valasek, “Adaptive Dynamic Inversion Control of a Linear Scalar Plant with Constrained Control Inputs,” *Proceedings of the American Control Conference*, Portland, OR, June 2005, pp. 2064–2069.
- [8] N. Hovakimyan, E. Lavretsky, and A. Sasane, “Dynamic Inversion for Nonaffine-in-Control Systems Via Time-Scale Separation: Part I,” *Proceedings of the American Control Conference*, Portland, OR, June 2005, pp. 3542–3547.
- [9] N. Hovakimyan, E. Lavretsky, and C. Cao, “Dynamic Inversion of Multiinput Nonaffine Systems Via Time-Scale Separation,” *Proceedings of the American Control Conference*, Minneapolis, MN, June 2006, pp. 3594–3599.

- [10] E. Lavretsky and N. Hovakimyan, "Adaptive Dynamic Inversion for Nonaffine-in-Control Systems Via Time-Scale Separation: Part II," *Proceedings of the American Control Conference*, Portland, OR, June 2005, pp. 3548–3553.
- [11] J. Buffington and A. Sparks, "Comparison of Dynamic Inversion and LPV Tailless Flight Control Law Designs," *Proceedings of the American Control Conference*, vol. 2, Philadelphia, PA, June 1998, pp. 1145–1149.
- [12] X.-. J. Liu, F. Lara-Rosano, and C. W. Chan, "Model-Reference Adaptive Control Based on Neurofuzzy Networks," *IEEE Trans. Syst., Man, Cybern. C*, vol. 34, no. 3, pp. 302–309, August 2004.
- [13] A. Calise and R. Rysdyk, "Nonlinear Adaptive Flight Control Using Neural Networks," *IEEE Control System Magazine*, vol. 18, no. 6, pp. 14–25, December 1998.
- [14] J. Leitner, A. Calise, and J. V. R. Prasad, "Analysis of Adaptive Neural Networks for Helicopter Flight Controls," *AIAA Journal of Guidance, Control, and Dynamics*, vol. 20, no. 5, pp. 972–979, September 1997.
- [15] Y. Shin, "Neural Network Based Adaptive Control for Nonlinear Dynamic Regimes," Ph.D. dissertation, Georgia Technical Institute, November 2005.
- [16] E. Lavretsky and N. Hovakimyan, "Adaptive Compensation of Control Dependent Modeling Uncertainties Using Time-Scale Separation," *Proceedings of the Conference on Decision and Control, and the European Control Conference*, Seville, Spain, December 2005, pp. 2230–2235.
- [17] B. Xian, D. M. Dawson, M. S. de Queiroz, and J. Chen, "A Continuous Asymptotic Tracking Control Strategy for Uncertain Nonlinear Systems," *IEEE Transactions on Automatic Control*, vol. 49, no. 7, pp. 1206–1211, July 2004.
- [18] P. M. Patre, W. MacKunis, C. Makkar, and W. E. Dixon, "Asymptotic Tracking for Systems with Structured and Unstructured Uncertainties," *Proceedings of the Conference on Decision and Control*, San Diego, CA, December 2006, pp. 441–446.
- [19] Z. Cai, M. S. de Queiroz, and D. M. Dawson, "Robust Adaptive Asymptotic Tracking of Nonlinear Systems with Additive Disturbance," *IEEE Transactions on Automatic Control*, vol. 51, no. 3, pp. 524–529, March 2006.
- [20] B. Xian, M. S. de Queiroz, and D. M. Dawson, *A Continuous Control Mechanism for Uncertain Nonlinear Systems in Optimal Control, Stabilization, and Nonsmooth Analysis*, Heidelberg, Germany: Springer-Verlag, 2004.
- [21] X. Zhang, A. Behal, D. M. Dawson, and B. Xian, "Output Feedback Control for a Class of Uncertain MIMO Nonlinear Systems with Nonsymmetric Input

- Gain Matrix,” *Proceedings of the Conference on Decision and Control, and the European Control Conference*, Seville, Spain, December 2005, pp. 7762–7767.
- [22] M. L. McIntyre, W. E. Dixon, D. M. Dawson, and I. D. Walker, “Fault Identification for Robot Manipulators,” *IEEE Transactions on Robotics and Automation*, vol. 21, no. 5, pp. 1028–1034, October 2005.
- [23] S. Gupta, D. Aiken, G. Hu, and W. E. Dixon, “Lyapunov-Based Range and Motion Identification for a Nonaffine Perspective Dynamic System,” *Proceedings of the American Control Conference*, Minneapolis, MN, June 2006, pp. 4471–4476.
- [24] W. E. Dixon, Y. Fang, D. M. Dawson, and T. J. Flynn, “Range Identification for Perspective Vision Systems,” *IEEE Transactions on Automatic Control*, vol. 48, no. 12, pp. 2232–2238, December 2003.
- [25] A. Behal, D. M. Dawson, W. E. Dixon, and Y. Fang, “Tracking and Regulation Control of an Underactuated Surface Vessel with Nonintegrable Dynamics,” *Proceedings of the Conference on Decision and Control*, vol. 3, Sydney, Australia, December 2000, pp. 2150–2155.
- [26] Center, J. A. V. N. T. S., “Vulnerability Assessment of the Transport Infrastructure Relying on the Global Positioning System,” Report, Office of the Assistant Secretary for Transportation Policy, U.S. Department of Transportation, August 2001.
- [27] G. Hu, S. Mehta, N. R. Gans, W. E. Dixon, "Daisy Chaining Based Visual Servo Control Part I: Adaptive Quaternion-Based Tracking Control ," *Proceedings of the IEEE Multi-conference on Systems and Control*, Singapore, October 2007, pp. 1474–1479.
- [28] G. Hu, N. R. Gans, S. Mehta, W. E. Dixon, "Daisy Chaining Based Visual Servo Control Part II: Extensions, Applications and Open Problems," *Proceedings of the IEEE Multi-conference on Systems and Control*, Singapore, October 2007, pp. 729–734.
- [29] Roberts, J. M., Corke, P. I., and Buskey, G., “Low-Cost Flight Control System for a Small Autonomous Helicopter,” *Proceedings of the Australasian Conference on Robotics and Automation*, Auckland, New Zealand, November, 2002.
- [30] Zhang, H. and Ostrowski, J., “Visual Servoing with Dynamics: Control of an Unmanned Blimp,” *Proceedings of the IEEE International Conference on Robotics and Automation*, vol. 1, May 1999, pp. 618–623.
- [31] Sharp, C. S., Shakernia, O., and Sastry, S. S., “A Vision System for Landing an Unmanned Aerial Vehicle,” *Proceedings of the IEEE International*

- Conference on Robotics and Automation (ICRA)*, Seoul, Korea, 2001, pp. 1720–1727.
- [32] Bernatz, A., and Thielecke, F., “Navigation of a Low Flying VTOL Aircraft With the Help of a Downwards Pointing Camera,” *Proceedings of the AIAA Guidance, Navigation, and Control Conference*, Providence, RI, August 2004.
- [33] Yuan, Z., Gong, Z., Wu, J., Chen, J., and Rao, J., “A Real-Time Vision-based Guided Method for Autonomous Landing of a Rotor-craft Unmanned Aerial Vehicle,” *Proceedings of the IEEE International Conference on Mechatronics & Automation*, Niagara Falls, Canada, July 2005, pp 2212–2215.
- [34] Wu, A. D., Johnson, E. N., and Proctor, A. A., “Vision-Aided Inertial Navigation for Flight Control,” *Journal of Aerospace Computing, Information, and Communication*, vol. 2, September 2005, pp. 348–360.
- [35] Schulz, H.-W., Buschmann, M., Krüger, L., Winkler, S., and Vörsmann, P., “Vision-Based Autonomous Landing for Small UAVs – First Experimental Results,” *Infotech@Aerospace*, Arlington, Virginia, September, 2005.
- [36] Jones, C. G., Heyder-Bruckner, J. F., Richardson, T. S., and Jones, D. C., “Vision-based Control for Unmanned Rotorcraft,” *Proceedings of the AIAA Guidance, Navigation, and Control Conference*, AIAA-2006-6684, Keystone, CO, August 2006.
- [37] Saripalli, S., Montgomery, J. F., and Sukhatme, G. S., “Visually Guided Landing of an Unmanned Aerial Vehicle,” *IEEE Transactions on Robotics and Automation*, vol. 19, No. 3, June 2003, pp. 371–380.
- [38] Chatterji, G. B., Menon, P. K., and Sridhar, B., “Vision-Based Position and Attitude Determination for Aircraft Night Landing,” *Journal of Guidance, Control, and Dynamics*, 1998 vol. 21, No. 1, pp. 84–92.
- [39] Proctor, A. A., and Johnson, E. N., “Vision-only Approach and Landing,” *Proceedings of the AIAA Guidance, Navigation, and Control Conference*, AIAA-2005-5871, San Francisco, CA, August 2005.
- [40] Liu, T., and Fleming, G., “Videogrammetric Determination of Aircraft Position and Attitude for Vision-Based Autonomous Landing,” *AIAA Aerospace Sciences Meeting and Exhibit*, AIAA-2006-1437, Reno, NV, January 2006.
- [41] Shakernia, O., Y. Ma, Koo, T. J., and Sastry, S., “Landing an Unmanned Air Vehicle: Vision Based Motion Estimation and Nonlinear Control,” *Asian Journal of Control*, vol 1, pp. 128–145.
- [42] Jianchao, Y., “A New Scheme of Vision Based Navigation for Flying Vehicles - Concept Study and Experiment Evaluation,” *Proceedings of the IEEE*

International Conference on Control, Automation, Robotics And Vision (ICARV), Singapore, December 2002, pp. 643–648.

- [43] Kim, J., “Autonomous Navigation for Airborne Applications,” Ph.D. Dissertation, Department of Aerospace, Mechanical and Mechatronic Engineering, The University of Sydney, Sydney, Australia, May 2004.
- [44] Webb, T. P., Prazenica, R. J., Kurdila, A. J., and Lind, R., “Vision-Based State Estimation for Uninhabited Aerial Vehicles,” *Proceedings of the AIAA Guidance, Navigation, and Control Conference*, AIAA-2005-5869, San Francisco, CA, August 2005.
- [45] Prazenica, R. J., Watkins, A., Kurdila, A. J., Ke, Q. F., and Kanade, T., “Vision-Based Kalman Filtering for Aircraft State Estimation and Structure from Motion,” *Proceedings of the AIAA Guidance, Navigation, and Control Conference*, AIAA-2005-6003, San Francisco, CA, August 2005.
- [46] Caballero, F., Merino, L., Ferruz, J., and Ollero, A., “Improving Vision-Based Planar Motion Estimation for Unmanned Aerial Vehicles Through Online Mosaicing,” *Proceedings of the IEEE International Conference on Robotics and Automation (ICRA)*, May 2006, pp. 2860–2865.
- [47] Koch, A., Wittich, H., and Thielecke, F., “A Vision-Based Navigation Algorithm for a VTOL-UAV,” *Proceedings of the AIAA Guidance, Navigation, and Control Conference*, AIAA-2006-6546, Keystone, CO, August 2006.
- [48] Barber, D. B., Griffiths, S. R., McLain, T. W., and Beard, R. W., “Autonomous Landing of Miniature Aerial Vehicles,” *Journal of Aerospace Computing, Information, and Communication*, vol. 4, May 2007, p. 770.
- [49] Trisiripisal, P., Parks, M. R., Abbot, A. L., Liu, T., and Fleming, G. A., “Stereo Analysis for Vision-based Guidance and Control of Aircraft Landing,” *Proceedings of the AIAA Aerospace Sciences Meeting and Exhibit*, AIAA-2006-1438, Reno, Nevada, January 2006.
- [50] A. Chiuso, P. Favaro, H. Jin, and S. Soatto, “Structure from Motion Causally Integrated Over Time,” *IEEE Transactions on Pattern Analysis and Machine Intelligence*, vol. 24, pp. 523–535, 2002.
- [51] H. Kano, B. K. Ghosh, and H. Kanai, “Single Camera Based Motion and Shape Estimation Using Extended Kalman Filtering,” *Mathematical and Computer Modelling*, vol. 34, pp. 511–525, 2001.
- [52] L. Matthies, T. Kanade, and R. Szeliski, “Kalman Filter-Based Algorithm for Estimating Depth from Image Sequence,” *International Journal of Computer Vision*, vol. 3, pp. 209–236, 1989.

- [53] S. Soatto, R. Frezza, and P. Perona, "Motion Estimation Via Dynamic Vision," *IEEE Transactions on Automatic Control*, vol. 41, pp. 393–413, 1996.
- [54] X. Chen and H. Kano, "State Observer for a Class of Nonlinear Systems and its Application to Machine Vision," *IEEE Transactions on Automatic Control*, vol. 49, no. 11, pp. 2085–2091, 2004.
- [55] X. Chen and H. Kano, "A New State Observer for Perspective Systems," *IEEE Transactions on Automatic Control*, vol. 47, no. 4, pp. 658–663, 2002.
- [56] W. E. Dixon, Y. Fang, D. M. Dawson, and T. J. Flynn, "Range Identification for Perspective Vision Systems," *IEEE Transactions on Automatic Control*, vol. 48, no. 12, pp. 2232–2238, 2003.
- [57] M. Jankovic and B. K. Ghosh, "Visually Guided Ranging from Observations of Points, Lines and Curves Via an Identifier Based Nonlinear Observer," *Systems and Control Letters*, vol. 25, pp. 63–73, 1995.
- [58] D. Karagiannis and A. Astolfi, "A New Solution to the Problem of Range Identification in Perspective Vision Systems," *IEEE Transactions on Automatic Control*, vol. 50, pp. 2074–2077, 2005.
- [59] L. Ma, Y. Chen, and K. L. Moore, "Range Identification for Perspective Dynamic System with Single Homogeneous Observation," *Proceedings of the IEEE International Conference on Robotics Automation*, 2004, pp. 5207–5212.
- [60] —, "Range Identification for Perspective Dynamic System Using Linear Approximation," *Proceedings of the IEEE International Conference on Robotics Automation*, 2004, pp. 1658–1663.
- [61] Ashley, H., and Landahl, M., *Aerodynamics of Wings and Bodies*, Dover Publications, Inc., 1985.
- [62] Z. Cai, M. S. de Queiroz, D. M. Dawson, and B. Xian, "Adaptive Asymptotic Tracking of Parametric Strict-Feedback Systems in the Presence of Additive Disturbances," *43rd IEEE Conference on Decision and Control*, December 14–17, 2004.
- [63] L. Duan, W. Lu, F. Mora-Camino, and T. Miquel, "Flight-Path Tracking Control of a Transportation Aircraft: Comparison of Two Nonlinear Design Approaches," *Proceedings of the Digital Avionics Systems Conference*, Portland, OR, October 2006, pp. 1–9.
- [64] I. Szaszi, B. Kulcsar, G. J. Balas, and J. Bokor, "Design of FDI Filter for an Aircraft Control System," *Proceedings of the American Control Conference*, Anchorage, AK, May 2002, pp. 4232–4237.
- [65] Department of Transportation, "Airworthiness Standards: Transport Category Airplanes," *Federal Aviation Regulations - Part 25*, Washington, DC, 1996.

- [66] F. L. Lewis, C. T. Abdallah, and D. M. Dawson, *Control of Robot Manipulators*, New York, NY: MacMillan, 1993.
- [67] B. S. Davis, T. Denison, and J. Kaung, "A Monolithic High-g SOI-MEMS Accelerometer for Measuring Projectile Launch and Flight Accelerations," *Proceedings of the Conference on Sensors*, Vienna, Austria, October 2004, pp. 296–299.
- [68] V. Janardhan, D. Schmitz, and S. N. Balakrishnan, "Development and Implementation of New Nonlinear Control Concepts for a UA," *Proceedings of the Digital Avionics Systems Conference*, Salt Lake City, UT, October 2004, pp. 12.E.5–12I–10.
- [69] T. Wagner and J. Valasek, "Digital Autoland Control Laws Using Quantitative Feedback Theory and Direct Digital Design," *AIAA Journal of Guidance, Control, and Dynamics*, vol. 30, no. 5, pp. 1399–1413, September 2007.
- [70] M. Bodson, "Multivariable Adaptive Algorithms for Reconfigurable Flight Control," *Proceedings of the Conference on Decision and Control*, Lake Buena Vista, FL, December 1994, pp. 12.E.5–12I–10.
- [71] B. J. Bacon, A. J. Ostroff, and S. M. Joshi, "Reconfigurable NDI Controller Using Inertial Sensor Failure Detection & Isolation," *IEEE Transactions on Aerospace Electronic Systems*, vol. 37, no. 4, pp. 1373–1383, Oct. 2001.
- [72] G. Tao, *Adaptive Control Design and Analysis*, S. Haykin, Ed., New York: Wiley-Interscience, 2003.
- [73] D. Dawson, M. Bridges, and Z. Qu, *Nonlinear Control of Robotic Systems for Environmental Waste and Restoration*, Englewood Cliffs, NJ: Prentice Hall PTR, 1995.
- [74] H. K. Khalil, *Nonlinear Systems, Third Edition*, Upper Saddle River, NJ: Prentice Hall, 2002.
- [75] P. M. Patre, W. MacKunis, C. Makkar, and W. E. Dixon, "Asymptotic Tracking for Systems with Structured and Unstructured Uncertainties," *IEEE Transactions on Control Systems Technology*, vol. 16, March 2008, pp. 373–379.
- [76] Kaiser, M. K., Gans, N. R., and Dixon, W. E., "Position and Orientation of an Aerial Vehicle through Chained, Vision-Based Pose Reconstruction," *Proceedings of the AIAA Guidance, Navigation, and Control Conference*, Keystone, CO, 2006.
- [77] Kaiser, M. K., Gans, N. R., and Dixon, W. E., "Localization and Control of an Aerial Vehicle through Chained, Vision-Based Pose Reconstruction," *Proceedings of the American Control Conference*, New York, NY, 2007.

- [78] Longuet-Higgins, H., “A Computer Algorithm for Reconstructing a Scene from Two Projections,” *Nature*, Sept. 1981, pp. 133–135.
- [79] Hartley, R., *Computer Vision Proc. of 1992 European Conference on Computer Vision, Lecture Notes in Computer Sciences*, New York: Springer-Verlag, 1992.
- [80] Nister, D., “An Efficient Solution to the Five-Point Relative Pose Problem,” *IEEE Transactions on Pattern Analysis and Machine Intelligence*, vol. 26, June 2004, pp. 756–770.
- [81] Ma, Y., Soatto, S. Kosecká, J., and Sastry, S., *An Invitation to 3-D Vision*, New York: Springer, 2004.
- [82] Faugeras, O., and Lustman, F., “Motion and Structure from Motion in a Piecewise Planar Environment,” *International Journal of Pattern Recognition and Artificial Intelligence*, vol. 2, No. 3, 1988, pp. 485–508.
- [83] Zhang, Z., and Hanson, A., “3D Reconstruction Based on Homography Mapping,” *Proceedings of the ARPA Image Understanding Workshop*, Palm Springs, CA, 1996.
- [84] S. Soatto and P. Perona, “Reducing "Structure from Motion": A General Framework for Dynamic Vision Part 1: Modeling,” *IEEE Transactions on Pattern Analysis and Machine Intelligence*, vol. 20, no. 9, pp. 933–942, 1998.
- [85] ———, “Reducing "Structure from Motion": A General Framework for Dynamic Vision Part 2: Implementation and Experimental Assessment,” *IEEE Transactions on Pattern Analysis and Machine Intelligence*, vol. 20, no. 9, pp. 943–960, 1998.
- [86] R. Y. Tsai and T. S. Huang, “Estimating Three-Dimensional Motion Parameters of a Rigid Planar Patch,” *IEEE Transactions on Acoustics, Speech, & Signal Processing*, vol. 29, no. 6, pp. 1147–1152, 1981.
- [87] D. Aiken, S. Gupta, G. Hu, and W. E. Dixon, “Lyapunov-Based Range Identification for a Paracatadioptric System,” *Proceedings of the IEEE Conference on Decision and Control*, 2006, pp. 3879–3884.
- [88] L. Ma, Y. Chen, and K. L. Moore, “Range Identification for Perspective Dynamic Systems with 3D Imaging Surfaces,” *Proceedings of the American Control Conference*, 2005, pp. 3671–3675.
- [89] S. Gupta, D. Aiken, G. Hu, and W. E. Dixon, “Lyapunov-Based Range and Motion Identification for a Nonaffine Perspective Dynamic System,” *Proceedings of the American Control Conference*, 2006, pp. 4471–4476.
- [90] J. J. Slotine and W. Li, *Applied Nonlinear Control*. Englewood Cliffs, NJ: Prentice Hall, 1991.

BIOGRAPHICAL SKETCH

Kent Kaiser received a B.S. degree in aerospace engineering from Auburn University in 1990, an M.S. degree in mechanical engineering from the University of Houston in 1995, and completed coursework towards an additional M.S. degree in aerodynamics and propulsion engineering from Cal Poly Pomona. He has nearly 20 years work experience within the aerospace industry, which includes his current employment with Air Force Research Labs (AFRL), as well as previous employment with Lockheed Martin Corporation in Houston, TX, Palmdale, CA, and Marietta, GA. Some of his research interests include system identification, aerodynamic performance based design, flight dynamics and control, neural net-based adaptive control, proper orthogonal decomposition (POD) for fluidic modeling and flow control, robust control, micro-UAVs, linear matrix inequality (LMI) control, nonlinear dynamic inversion methods for aircraft control, vision-based estimation, guidance, and control, and cooperative control.